CONSERVED NUCLEAR MORPHOLOGY IDENTIFIES FUNCTIONAL RADIAL GLIA NEURAL PROGENITORS

Soriano-Esqué J.P.[1,2], Borau C.[3,4], Sortino R.[5,6], Garma L.D.[7], Ortega J.A.[1,2], Asín J.[8], Alcántara S.[1,2,*]

Affiliations:

[1] Department of Pathology and Experimental Therapeutics, Institute of Neurosciences, University of Barcelona, L'Hospitalet de Llobregat, Barcelona 08907, Spain.

[2] Neurodevelopmental Disorders Group, NeuroBell, Institut d'Investigació Biomèdica de Bellvitge (IDIBELL), L'Hospitalet de Llobregat, 08908, Spain.

[3] Centro Universitario de la Defensa de Zaragoza, Zaragoza, 50090, Spain.

[4] Multiscale in Mechanical and Biological Engineering (M2BE), Mechanical Engineering Department, University of Zaragoza, Zaragoza, 50018, Spain.

[5] Institute for Bioengineering of Catalonia (IBEC), The Barcelona Institute of Science and Technology, Carrer de Baldiri Reixac, 10-12, 08028, Barcelona, Spain.

[6] CIBER-BBN, ISCIII, Carrer de Melchor Fernández Almagro, 3, 28029, Madrid, Spain.

[7] Centro Nacional de Investigaciones Oncológicas–CNIO, Melchor Fernández Almagro 3, Madrid, 28029, Spain.

[8] Department of Statistical Methods, University of Zaragoza, Zaragoza, 50018, Spain.

SUMMARY

Radial glia (RG) bipolar morphology is crucial for maintaining their integrity and function as neural stem cell and substrate for neural migration in the embryonic brain. We previously described that astrocytes dedifferentiate into functional RG when cultured on a RG mimetic micro3D platform, although we ignore the underlying mechanotransducive effectors. Here we analyzed the role of nuclear deformation to unravel their mechanotransducive effectors on RG induction. A multivariate generalized linear model developed for fitting RG identity probability revealed the existence of intrinsic nuclear constraints that allow a precise range of permitted RG nuclear morphologies, which are associated with particular nuclear calcium dynamics. Interestingly, RG nuclear constraints are conserved *in vivo*, *in vitro* and through evolution. Our work provides a framework for studying the interplay between nuclear mechanics, morphology, and cell fate decisions, offering a novel approach for RG identification and differentiation studies.

KEYWORDS

biomimetic materials, statistical modeling, neural development, nuclear mechanobiology, calcium imaging, cerebral cortex, cortical evolution

INTRODUCTION

During embryonic development, biochemical and mechanical cues from the microenvironment shape neural tube formation and control neural progenitors' proliferation, functional properties and fate decisions[1-3]. Radial glia (RG) are the principal neural progenitor cells (NPC) that generate neurons and glial cells, directly or through transit amplifying intermediate progenitors (IP)[4,5]. RG are bipolar cells spanning the cerebral wall from the ventricular (apical) to the pial (basal) surfaces. Apical-basal anchorage generates mechanical tensions and localized exposure to extracellular and mechanical signals, which are key for maintaining nuclear interkinetic migration during cell cycle, RG structural integrity and function, including serving as scaffolds for neuronal migration[1,2]. Detachment from the ventricle or the pia while retaining apical-basal polarity generates outer RG (oRG) or truncated RG (tRG) respectively, which maintain self-renewing potential[3]. On the contrary, complete detachment generates nonpolar IP expressing T-box transcription factor TBR2/EOMES (TBR2)[6], neural/glial antigen 2 (NG2) proteoglycan[7], or GS Homeobox 2 transcription factor (GSX2)[8], which exhibit different fate potentiality. At the end of neurogenesis, RG directly, or indirectly through intermediate glial progenitors, transforms into astrocytes[9]. These developmental transitions seem to occur via a transcriptional continuum, and frequently, cells assume their final fate post-mitotically by non-cell autonomous environmental factors[10,3]. Importantly, RG-astrocyte differentiation is bidirectional[9], and astrocyte differentiation can be partially reverted into RG-like progenitors after a lesion[10]. In fact, a subgroup of astrocytes expressing glial fibrillary acidic protein (GFAP) and SRY-box transcription factor 2 (Sox2) were recently identified as quiescent adult neural stem cells (NSC) with neurogenic capacity, characteristics shared with their RG embryonic counterparts[11].

Biomaterial strategies mimicking the physical characteristics of the tissue *in vivo* have been used for mechanobiology studies where effects of mechanical cues from the niche on NSC differentiation have been analyzed[12,13]. We have previously demonstrated an essential role of local physical constraints in inducing astrocyte transformation into functional RG by using ln2PMMA, a non-biodegradable micro3D RG biomimetic material. Astrocytes cultured in ln2PMMA adopt RG bipolar morphology, express paired box 6 (Pax6) and Sox2 transcription factors and support neuronal migration[14,15]. Ln2PMMA is a synthetic scaffold of poly (methyl methacrylate) (PMMA) with 2µm linear grooves that mimics RG topology, the hydrophobicity and negative charge of RG plasma membrane. Both anisotropic topology, topography and surface properties are essential, as thicker grooves (5-20µm), flat PMMA, or hydrophilic and positively charged substrates as chitosan, even with 2µm groove topographies, failed to induce functional RG[14,16].

These results highlight that biophysical signals mimicking the RG embryonic niche are sufficient to induce some RG functional phenotypes. However, the mechanosensing and mechanotransducive mechanisms underlying this process are largely unknown.

Mechanotransduction is the conversion of mechanical forces generated by the microenvironment into biochemical signals and cellular response[17]. Cell adhesion proteins in the cell membrane generate tensions through the cytoskeleton that translate environmental mechanical signals to the nucleus. Subsequent nuclear deformation, changes in nuclear envelope composition and chromatin remodeling are critical in translating biomechanical signals into changes in gene expression and cell fate/behavior[18-20]. RG mechanical properties are regulated by centrosome anchoring to the apical membrane[21] and nuclear deformation is essential for the interkinetic nuclear migration[22], affecting their proliferative and neurogenic capacity. Moreover, mechanosensitive cation channels and calcium dynamics regulate the proliferative capacity of RG and other NPC[23,24], highlighting the relevance of biomechanical and bioelectrical mechanisms for neurogenesis and neural development.

Here, we investigate the role of nuclear morphology in mechanically induced astrocyte-RG transitions by the development of a multivariate generalized linear model for RG identification and the use of the RG mimetic platform ln2PMMA. With this approach, we interrogate the physiological relevancy of RG nuclear constraints, the evolutive conservation of these constraints between mice and human, and the disrupting effect of standard cultures on flat substrates.

RESULTS

Ln2PMMA changes the nuclear morphology of Astrocyte – RG lineage cells

To analyze whether mechanical regulation of nuclear morphology is relevat for inducing RG fate we used the ln2PMMA platform, wich microtopograpy mimic RG niche structural anisotropy, and forces cultured astrocytes to adopt the bypolar morphology, Pax6 expression and functional characteristics of RG[14,15]. We grew astrocyte-enriched cultures on uncoated ln2PMMA and flat borosilicate glass (control) substrates for 3 days in vitro (3DIV) (**Figure 1A**). Nuclear morphology parameters (area and eccentricity) of Hoechst stained nuclei of a total of 3855 cells (2135 in control and 1720 in ln2PMMA) were analyzed and associated to cell-type markers expression, using a custom-made MATLAB algorithm (see material and methods, **Figure 1B**). We identified different cell types across glial lineage with the following markers: the intermediate filaments GFAP for astrocytes and nestin for immature astrocytes/RG, the transcription factors Sox2 for NSC, Pax6 for RG, and for IP the proteoglycan NG2 for oligodendrocyte progenitors

(OPC), and Gsx2 for tripotential IP (**Figure 1C**). In the same line than our previous studies[14,15], we observed that the proportion of GFAP+ astrocytes was significantly reduced while Pax6+ RG was significantly increased in ln2PMMA with respect to control substrates (**Figure 1D**).

To explore the effect of ln2PMMA on the nuclear area and eccentricity associated to each glial cell type we performed multivariate kernel density estimation. A nonparametric technique for population density estimation that assigns density probability regions for each cell marker, based on shared area and eccentricity (**Figure 1E**). We found no statistically significant differences between marker distributions; therefore we conducted t-tests to compare nuclear parameters individually between substrates within the same cell type. This analysis showed that nuclei from nestin+, GFAP+, Pax6+ and Sox2+ cells were significantly deformed in ln2PMMA, adopting more elongated shapes, while nuclei from NG2+ and Gsx2+ IP cells did not significantly change their morphology (**Table S1**). Together these data indicate that only cells from the direct astrocyte-RG lineage respond to ln2PMMA mechanical signals by changing their nuclear morphology. In line with other mechanosensitive cell types wich nucleus deform and orient as cells elongated under anisotropic forces, afecting chromatin organization and gene transcription[19,25,26].

Development of a generalized linear model to predict RG probability based on nuclear morphology parameters

We constructed a linear regression model to evaluate whether nuclear deformation constitutes a hallmark in mechanically driven RG induction. We defined prediction success as the ability to identify nuclei specific to RG, using nuclear area and eccentricity as predictors. The model relies on a binary response: RG or not RG, determined by the presence or absence of molecular markers indicative of the RG phenotype (Pax6+ or double Sox2+/nestin+). Importantly, cell-cell interactions are essential determinants of cell shape, proliferation, differentiation, and growth, and can revert the effect of the mechanical signals from the substrate[15]. Moreover, interactions among groups of precursor cells facilitate their coordinated differentiation during development, the so-called community effect[27]. Therefore, we included cell density in addition to nuclear area and eccentricity as predictors to account for this community effect. We used generalized linear models with the logit function to link the binary response to the linear predictor and estimates the probability of an event. In our case, the event was identifying whether RG cells exhibited a specific nuclear morphology, using glial cultures grown in control and ln2PMMA substrates for 3DIV. We developed multiple models of increasing complexity, by adding, suppressing, or conditioning these variables based on substrate type. The best model was selected following the Akaike Information Criterion (AIC), aiming to

select the model that best explains the data with the fewest parameters. We refined the selected model using a step-by-step procedure to eliminate complex and non-significant terms. For example, by including cell density as an independent variable only in interactions, we reduced the AIC from 1313.062 to 1302.395 (**Table S2**). Most non-significant terms were eliminated (further details in methods); however, terms relevant only in specific substrate interactions were retained, even if they were non-significant in the counterpart substrate. This refinement further reduced the AIC to 1300.325, indicative of a better fitting. Despite this improvement, it came at the cost of a reduction in AUC (Area Under the Curve), which measures the ability of the model to distinguish between classes across all decision thresholds. This trade-off reflects the balance

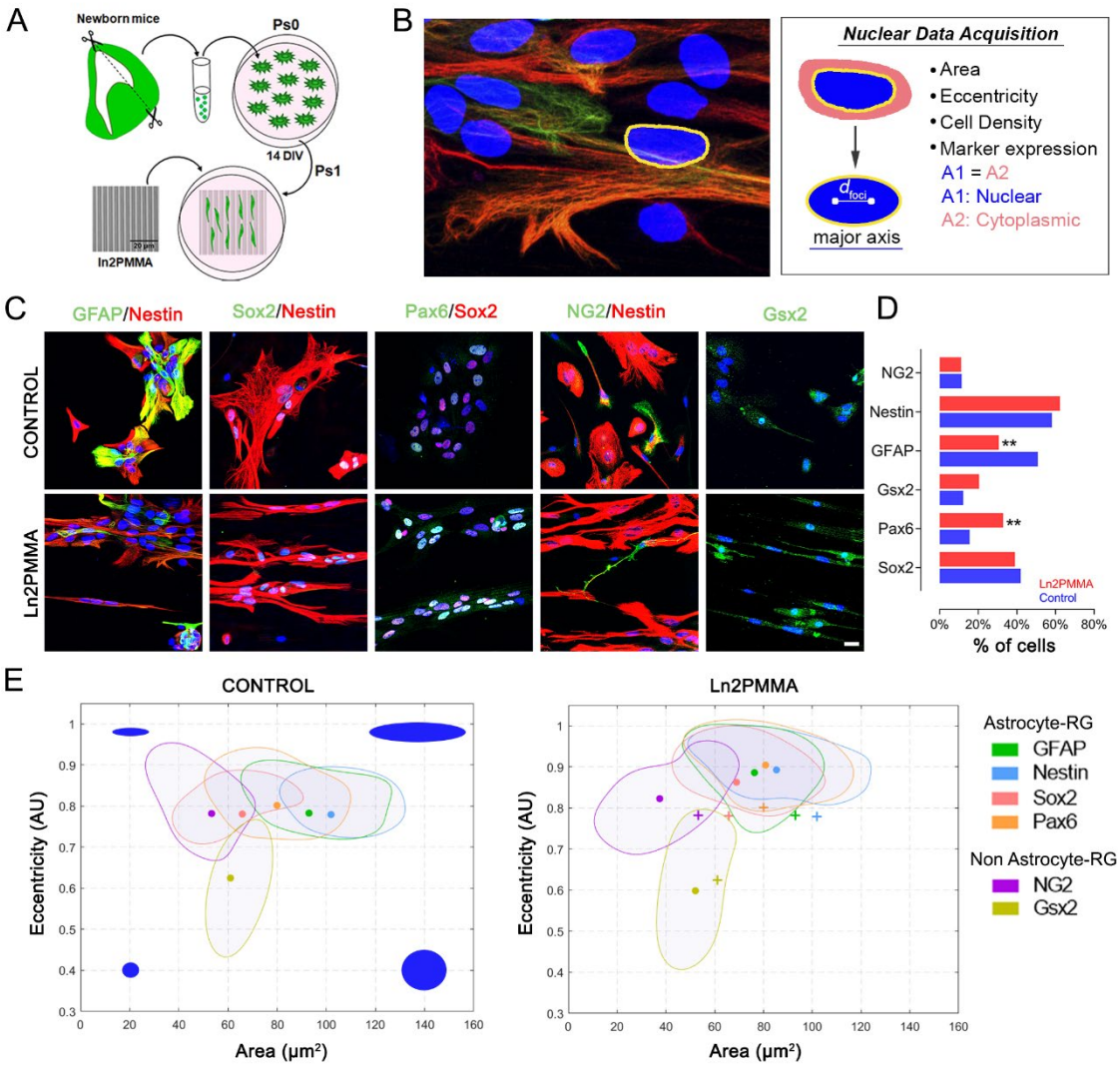

Figure 1: Glial cultures cell composition and nuclear morphology in control and ln2PMMA substrates. (A) Schematic diagram of cell culture protocol. **(B)** Schematics of nuclear data acquisition. **(C)** Representative pictures of primary cortical glial cells, grown in control and ln2PMMA substrates for 3DIV, labeled with different combinations of cell-specific markers for astrocytes (GFAP), immature astrocytes/RG (nestin), RG (Pax6), general stem cells (Sox2) and intermediate progenitors (NG2, Gsx2). Nuclei were stained with Hoechst (blue). Scale bar: 20μm. **(D)** Bar plot showing the percentage of different cell types in both control and ln2PMMA. **(E)** Density function probability plot with centroids representing the median values of eccentricity (y-axis) and area (x-axis) for each cell type. Blue shapes represent the reference of area-eccentricity combinations. Chi-square test **p<0.01.

between reducing model complexity and maintaining predictive accuracy. We obtained a general model AUC of 0.73, with substrate-specific AUCs of 0.77 for ln2PMMA and 0.67 for the control substrate (**Table 1, Figure 2A**).

Table 1. Summary of model performance and significant terms. Top rows show AIC value for the general model and AUC values divided by substrate, including lower and upper 95% confidence intervals (CI). Bottom rows show estimate values, standard error, z value and p-value for the selected terms of the model grouped by its substrate dependence. A: Area, E: Eccentricity and D: cell density. The full table is shown in the methods section.

Model	**AIC**	**AUC**	**Lower CI**	**Upper CI**
General	1300.325	0.73	0.7	0.76
Control		0.67	0.62	0.71
Ln2		0.77	0.73	0.81
Selected terms	**Estimate**	**Std. Error**	**z value**	**p-value**
Depe ndent on substrates				
Ln2PMMA	-9.45E+02	5.66E+02	-1.669	0.095
Control * E^3	-2.31E+02	8.84E+02	-0.261	0.794
Ln2PMMA * E^3	2.57E+03	7.32E+02	3.509	0.000
Ln2PMMA * A	-7.33E+00	4.74E+00	-1.546	0.122
Independent on substrates				
E^2 * D	5.15E+00	2.49E+00	2.068	0.039
A * D	-1.46E-01	4,13E-02	-3.522	0.000

For the different terms in the selected model, the sign of the estimated value indicates the direction of the prediction: positive values increase the probability of a specific RG nuclear morphology, while negative values decrease it. The z-value represents the relative weight or importance of each term in the model. Larger absolute z-values indicate a stronger impact of the corresponding term on the prediction. Finally, the relevance of each term is primarily determined by its p-value, which measures the statistical significance. A smaller p-value (e.g., < 0.05) suggests that the term is likely to have a meaningful contribution to the model, whereas larger p-values indicate weaker or negligible effects. The term associated with the ln2PMMA substrate alone did not meet the 5% significance level. However, in interaction with eccentricity, it demonstrated a substantial positive impact on the response (p-value < 0.01). As eccentricity increased, the probability of a nucleus being specific to RG cells became more defined. Therefore, in our modeling approach, we retained the effect of the ln2PMMA substrate on its own, as the term emerged during model construction and interacted with other variables. Similarly, we included the interaction between the control substrate and eccentricity, despite it not being statistically significant and showing a negative effect on the response (z-value=-2.61E-01) (**Table 1**). Nevertheless, the inclusion of cubic eccentricity in interaction with both substrates underscored the relevance of increased eccentricity induced by the ln2PMMA substrate in favoring a distinct nuclear morphology specific to

RG cells. Cell density was included in the model solely as an interacting variable. This approach reflects the impact of increased cell-cell interactions at higher cell densities, which can independently influence cell and nuclear morphologies regardless of the substrate. In our model, cell density demonstrated statistically significant interactions with area (p-value < 0.01) and eccentricity (p-value < 0.05), specifically in quadratic or cubic terms (**Table 1**).

The presence of substrate-dependent terms allowed splitting the model in two equations, one for control substrate (**eq. 1**) and another for ln2MMA substrate (**eq. 2**).

(1) $\mathrm{logit}(\ \mathrm{P}\big(\mathrm{y}=1\big|(\mathrm{X},\mathrm{Control})\big) = \beta_0 + \beta_A\mathrm{A} + \beta_{\mathrm{A}^2}\mathrm{A}^2 + \beta_{\mathrm{A}^3}\mathrm{A}^3 + \beta_{E^3C}\mathrm{E}^3 + \beta_{E^2*D}\mathrm{E}^2 * \mathrm{D} + \beta_{E*D^2}\mathrm{E} * \mathrm{D}^2 + \beta_{A*D}\mathrm{A} * \mathrm{D} + \beta_{A*D^2}\mathrm{A} * \mathrm{D}^2 + \beta_{A^2*D}\mathrm{A}^2 * \mathrm{D} + \beta_{A^2*D^2}\mathrm{A}^2 * \mathrm{D}^2$

(2) $\mathrm{logit}(\ \mathrm{P}\big(\mathrm{y}=1\big|(\mathrm{X},\mathrm{Ln2PMMA})\big) = \beta_0 + \beta_{0Ln2} + \beta_A\mathrm{A} + \beta_{\mathrm{A}^2}\mathrm{A}^2 + \beta_{\mathrm{A}^3}\mathrm{A}^3 + \beta_{E^3Ln2}\mathrm{E}^3 + \beta_{ALn2}A + \beta_{E^2*D}\mathrm{E}^2 * \mathrm{D} + \beta_{E*D^2}\mathrm{E} * \mathrm{D}^2 + \beta_{A*D}\mathrm{A} * \mathrm{D} + \beta_{A*D^2}\mathrm{A} * \mathrm{D}^2 + \beta_{A^2*D}\mathrm{A}^2 * \mathrm{D} + \beta_{A^2*D^2}\mathrm{A}^2 * \mathrm{D}^2$

The expression *logit (…)* represents the application of the linear predictor to estimate the probability of the response y=1 (success, previously defined as being RG), using the variables X = area, eccentricity and cell density on control or ln2PMMA substrates. In the model, *β* corresponds to estimated coefficients*, A* to area, *E* to eccentricity, and *D to* cell density. Specific terms depending on substrate are indicated as C for control and Ln2 for ln2PMMA.

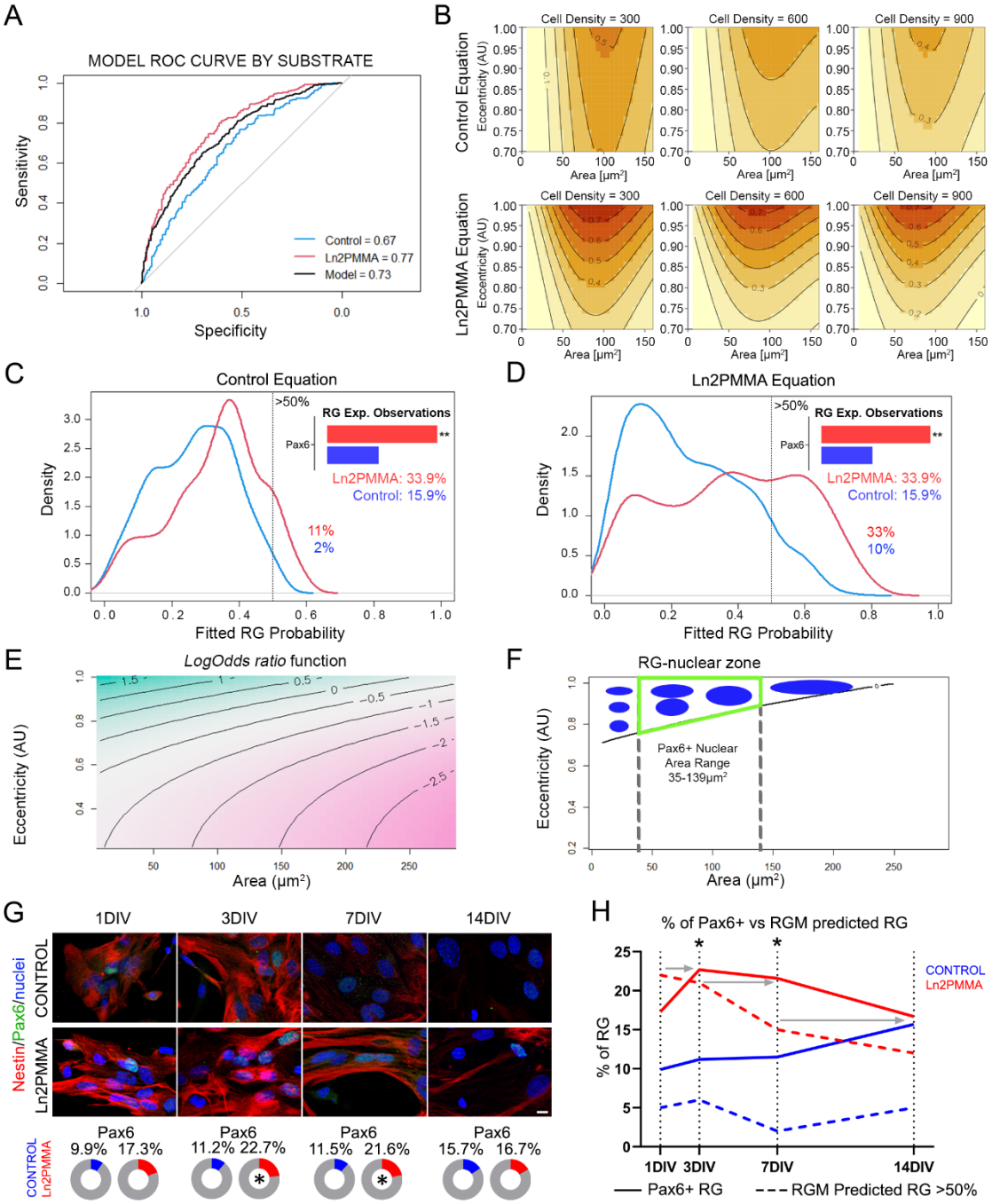

Figure 2: Model fitting and validation: identification of a RG-specific nuclear zone.
(A) ROC curves of the model: the general model ROC curve is shown in black, control equation in blue and ln2PMMA equation in red. Values in the legend show the AUC. **(B)** Surface plots of eccentricity (y-axis) and area (x-axis) of both model equations. Line curves represented the adjusted RG-probability at three different cell densities, 300, 600 and 900 cells/mm^2 in control and ln2PMMA. Density distribution of RG probabilities applying of control **(C)** and ln2PMMA **(D)** equations to the training dataset. Dashed lines delimitate the 0.5 probability threshold that stablishes RG identification. The numbers correspond to the percentage of cells with fitted probability over thershold of each case. Bars plot shows the proportion of cells expressing the Pax6 RG marker in the dataset. **(E)** Surface plot in function of area (x-axis) and eccentricity (y-axis) representing different levels of the LogOdds ratio function. **(F)** F(0) level of LogOdds ratio function (ascending black line) and representative RG nuclear morphologies. Vertical dashed lines delimitate the nuclear area range of Pax6+ cells. The theoretical RG nuclear zone is highlighted in green. **(G)** Validation results. Representative pictures of primary cortical glial cells cells grown on control and ln2PMMA for 1, 3, 7 and 14 DIV, labeled with RG lineage markers nestin (red) and Pax6 (green), and nuclei stained with Hoechst (blue). Pie charts showing the proportion of Pax6+ cells at each time point. **(H)** Plot comparing % calculated in base to Pax6+ cells (filled lines) or by the RGM model (dashed lines) at each time point. Gray arrows highlight the temporal shif of the RGM model predictions. Chi-square test, *p<0.05, **p<0.01.

The statistical model identify a RG-specific nuclear morphology

The analysis of surface plots showing area, eccentricity and adjusted probability curves at different cell densities, revealed a "*RG nuclear zone*" in which RG probability raises for medium sized and highly elongated nuclei, and is dynamically modulated by cell density (**Figure 2B**). However, the two equations, corresponding to control and ln2PMMA substrates (**eq.1** and **eq.2** respectively), resulted in different probability thresholds for the same nuclear morphology. This means that a nucleus with identical area and eccentricity values could be predicted as RG in one substrate condition but not in the other, raising the question of whether an RG-specific nuclear morphology truly exists. Thus, we evaluated the matching between control and ln2PMMA model equations predictions (stablishing the probability identification threshold of RG at 0.5), and the percentage of experimentally observed RG (Pax6+ cells) in the same control and ln2PMMA datasets used for model construction. The control equation predicted 2% of RG in control and 11% in ln2PMMA, values far below the experimental observations of 15.5% of pax6+ cells in control, and 32.9% in ln2PMMA (**Figure 2C**). In contrast, ln2PMMA equation predicted 10% of RG in control and 33% in ln2PMMA much closer to the experimentally observed values of Pax6+ cells in both substrates (15% and 33% respectively, **Figure 2D**). Hence, the model used from that time on was exclusively based on ln2PMMA equation and named Radial Glia Mimetic (RGM) model.

When applying the RGM model to different glial subtypes classified by marker expression in the dataset used for training the model, we observed a positive shift of RG probability curves for specific marker combinations in the ln2PMMA condition (**Figure S1**). The highest RG probability were observed for all marker convinations including Pax6+, followed by nestin+/Sox2+ cells in both substrates (**Figure S1 A-E**). Besides, RG probability for these cells dropes fron 0.8-0.51 in ln2PMMA to 0.15-0.22 in control substrate, according with the scarce presence of functional RG in standard glial cultures[14]. Besides their use as lineage markers, the expression of nestin or GFAP was not informative about the astrocyte-RG differentiation state, as RG predictions were quite similar (estimated percentage ranging between 0.49-0.43 in ln2PMMA and 0.11-0.08 in control substrate) (**Figure S1 F-I**). Other lineage marker combinations, with the inclusion of NG2 and Gsx2 markers, exhibit even lower RG probability (**Figure S1 J-P**). Together these results indicate that Pax6+ and double nestin+/Sox2+ marker combinations are strong predictors of RG identity, and suggest that despite their expression, the functional RG phenotype is not achieved in the absence of the apropiated mechanical cues. This is in line with the notion that cell differentiation occurs via a transcriptional continuum, and the final fate depends on non-cell autonomous environmental factors[10,3]. Moreover,

the presence of nestin and/or GFAP intermediate filaments in glial cells seems to proporcione mechanosensitivity, as they are required for the capacity to move along astrocytic-RG lineage in response to mechanical stimuli, and in their absence in cells have only a residual effect on RG probability (≤ 0.08, **Figure S1 N-P**).

The LogOdds ratio function F(0) identifies RG-intrinsic nuclear mechanical constrains

The accuracy of the RGM model, regardless of the culture substrate, suggests the presence of cell-intrinsic mechanical factors that constrain the range of possible nuclear shapes in functional RG progenitors. If this holds true, the specific terms of the ln2PMMA model equation may capture these intrinsic nuclear constraints, which are likely enhanced by the RG-mimetic properties of the ln2PMMA substrate. To identify those nuclear constraints, we calculated the odds ratio function, a standard measure for assessing relative changes between probabilities. Here, it is applied to measure changes in ln2PMMA over control equations. The odds ratio function was defined as follows:

(3) $Odds\ ratio = \frac{Odds\ (Ln2PMMA)}{Odds\ (Control)} = \frac{\mathrm{logit}(\ \mathrm{P}\left(\mathrm{y} = 1 \middle| (\mathrm{X}, Ln2PMMA)\right)}{\mathrm{logit}(\ \mathrm{P}\left(\mathrm{y} = 1 \middle| (\mathrm{X}, \mathrm{Control})\right)} = \exp(\beta_{0Ln2} + \beta_{E^3Ln2}\mathrm{E}^3 + \beta_{ALn2}A - \beta_{E^3C}\mathrm{E}^3)$

Since all common terms between the equations cancel out, the odds ratio (**eq. 3**) depends only on nuclear area and eccentricity, both of which are cell-intrinsic parameters. By applying the logarithm to the odds ratio (**eq. 4**), we obtain a bidimensional function that defines the effect of ln2PMMA as mimetic of the anisotropic embryonic RG niche, ensured compatibility with coefficients defined in linear regression models.

(4) $Log(Odds\ ratio) = LogOdds\ ratio(A, E) = \beta_{0Ln2} + \beta_{E^3Ln2}\mathrm{E}^3 + \beta_{ALn2}A - \beta_{E^3C}\mathrm{E}^3$

To analyze the behavior of the LogOdds ratio function, we created a surface plot at various levels of the function (**Figure 2E**). We defined the isolines of the LogOdds ratio function as lines in the plane defined by nuclear area and eccentricity that correspond to the same function value. When LogOdds ratio = 0, the resulting line, F(0), delineated the boundary of area and eccentricity at which the RGM model consistently elevated the probability of a nucleus being classified as RG, regardless of the substrate type (control or ln2PMMA). This F(0) line likely reflects an intrinsic mechanical constraint within the cells, establishing a theoretical threshold for RG nuclear morphology. Using this threshold, we identified the nuclear morphologies permissible within the defined RG-nuclear zone, above F(0) and within the nuclear area range of Pax6+ RG in our cultures (min = 34.75 μm², max = 139 μm², **Figure 2F**). It is worth noting that due to the removal of relevant parameters in the LogOdds ratio function with respect to the RGM model, all

nuclei with >0.5 RG probability were above the F(0) threshold, but not all nuclei above F(0) were identified as RG by the RGM model.

RGM model validation

The validity of the model was tested in several independent and previously unseen glial cultures datasets at the timepoint used for constructing the model (3DIV), and in neuronal cultures. We confirmed the accuracy of RG detection in glial cultures (ln2PMMA: Pax6+ cells 22.7% and 21% of nuclei with RG p>0.5; Control: Pax6+ cells 11.2% and 6% of nuclei with RG p>0.5, **Figure 2 G;** 3DIV). Corroborating that in flat control substrate RGM RG probability is always lower than the corresponding for the proportion of Pax6+ cells. Moreover, RG probability in neuronal cultures was almost null (p≤ 0.02, **Figure S2**).

Nuclear deformation precedes gene expression changes in biomechanically induced astrocyte-RG transition

Knowing that RGM model accurately identify RG at 3DIV, we investigated the dynamics of nuclear deformation and Pax6 expression in control and ln2PMMA substrates from 1DIV to 14 DIV, wich encompass a complete cicle of astrocyte-RG-astrocyte transitions[15]. In our culture conditions, the proportion of Pax6+ cells in control substrate was relatively high, considering that no functional RG is present in standard glial cultures[14], and showed no significant differences over time in (9.9-15.7%). As expected, RGM model RG prediction in control substrate was stable over time, while significantly lower (5-10%) than the proportion of Pax6+ cells. In contrast, the proportion of Pax6+ RG in ln2PMMA varied with culture maturation, peaking significantly at 3 and 7DIV (22.7-21.6%), and resembling control substrate levels at the initial (1 DIV, 17.3%) and final (14 DIV, 16.7%) time points (**Figure 2G**). Accordingly, RGM model predictions in ln2PMMA substrate were higher but shifted to earlier time points, peaking at 1-3 DIV (22–21%) and steadily decreasing at 7 and 14 DIV (15–12%), while still remaining higher than those predicted in the corresponding control substrate (**Figure 2H**). Given that we used Pax6 expression at 3DIV as a RG marker to construct the RGM model, this temporal shift between the amount of RG identified by the two methods was puzzling. One possible explanation is that nuclear deformation could preceed Pax6 expression changes during astrocyte-to-RG transitions. If that was the case, the RGM model would be predictive of fate direction, detecting RG and those cells commited to be RG, while ignoring cells at the initial stages of differentiation but before Pax6 expression decay.

Ln2PMMA mechanical signals reduces lamins A-C/B1 ratio and increases nuclear β catenin in glial cells but not specifically in RG

We considerer nuclear mechanotransduction to gain more insight into the intracellular mechanisms that control mechanically driven RG induction. The expression of lamin isoforms, the principal components of the nuclear lamina, differentialy change during developmental progression and is associated with cellular mechanical adaptations to the microenvironment[28,29]. To evaluate whether the relative expression of lamin genes in mouse RG-astrocyte lineage cells change during cerebral cortex development, we performed a metanalysis of publicly available single cell transcriptomics datasets[30]. We found an inverse correlation between Lmna (codifying for lamin A and C proteins) and Lmnb1 (codifying for lamin B1 protein) expression from E17 onwards (**Figure 3A**; see methods an **Figure S3** for details in the selection of RG-astrocyte lineage cells). These expression changes lead to a sustained increase in Lmna/Lmnb1 ratio during late embryonic and early postnatal brain development, coincidental with the increase in Gfap (codifying for GFAP protein) expression and astrocyte maturation. Therefore, we analyzed whether changes in lamins A-C/B1 ratio were involved in nuclear deformation observed during biomechanical driven astrocyte-RG transitions. For that, we immunostained glial cultures with lamins A-C and lamin B1 antibodies and analyzed the nuclear lamins A-C/B1 ratio at 1DIV, 3DIV and 7DIV (**Figure 3B**). At all times analyzed, nuclear lamins A-C/B1 ratio was significantly lower in ln2PMMA compared to the control substrate. However, the lamins ratio increased over time at similar rates in both substrates as the culture mature (**Figure 3C**). These data suggest that the nuclear lamina adapts its composition to ln2PMMA mechanical signals, and sustains these changes throughout the culture period. Then, we applied the RGM model to explore whether specific lamins A-C/B1 ratios were associated with increased RG probability. We observed a mild inverse correlation between the lamin A-C/B1 ratio and RG probability, despite no specific lamin A-C/B1 ratio was specificaly associated with increased RG probability (**Figure 3D-F**).

Mechanosensitive transcription factors, such as β-catenin, yes-associated protein (YAP) and the transcriptional coactivator with PDZ-binding motif (TAZ), adapt their subcellular distribution and activity in response to changes in forces and cellular morphology, and are also directly involved in RG organization and expansion[31,32,33,34,35,36,37]. Therefore, we wondered whether ln2PMMA biomechanical induction of RG affect β-catenin and YAP/TAZ expression or subcellular distribution. To address this, we immunostained glial cultures grown on control and ln2PMMA at 1DIV, 3DIV and 7DIV for β-catenin and YAP/TAZ. From subsequent confocal images we calculated the nuclear/cytoplasmic intensity ratio (Nuc/Cyto ratio) and performed a linear regression analysis to evaluate dynamic nuclear-cytoplasmic shuttling over time (**Figure 3G**). We found that β-catenin

subcellular distribution in glial cells was similar in both substrates at 1DIV. However, it shuttles out of the nucleus over time in culture in a significantly faster pace in the control (higher negative slope) than in In2PMMA substrate, which retained nuclear β-catenin along time (**Figure 3H**). These results point to sustained β-catenin nuclear signaling as one of the mecanotransduction mechanisms involved in In2PMMA RG induction, as β-catenin binding to Pax6 promoter induce its transcription[38]. Nevertheless, no specific nuclear-cytoplasmic ratio was predominatly associated with increased RG probability (**Figure 3I-K**). Conversely, we found no significant differences in YAP/TAZ subcellular distribution in glial cells between substrates and over time (**Figure 3L-M**). Together these data indicate that mechanically induced nuclear elongation, lower lamin A-C/B1 expression ratio and persistent β-catenin nuclear signaling facilitate but do not determine RG fate.

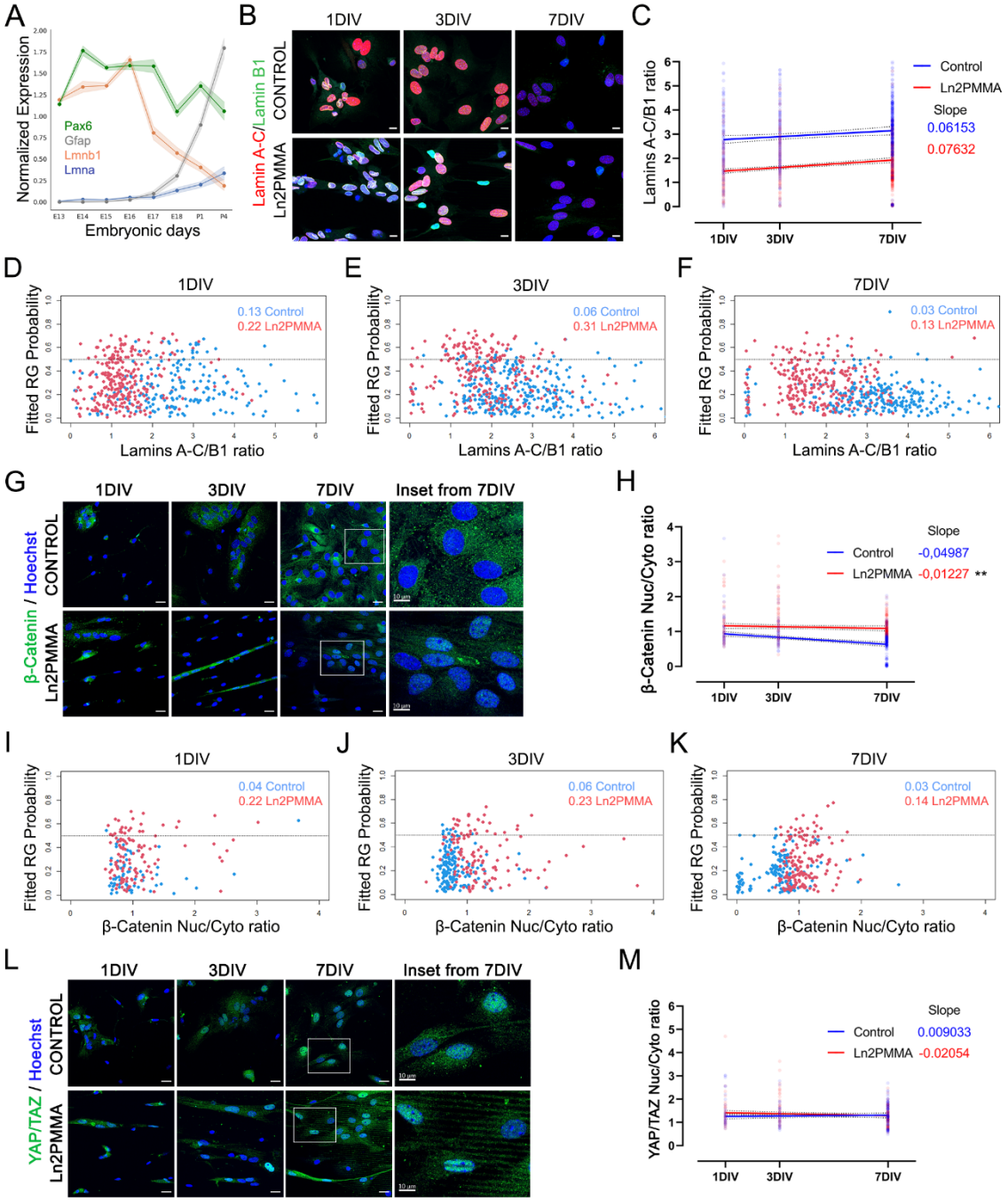

Figure 3: Ln2PMMA effect on lamins, β-catenin and YAP/TAZ expression and subcellular distribution across time in culture. (**A**) Plot showing a negative correlation between Lmnb1 and Lmna gene expression in RG-astrocyte lineage cells during brain development, normalized by the average of Lmna gene expression at E13 (data from Di Bella et al., 2021). (**B**) Confocal images of glial cells grown for 1-7 DIV on control and ln2PMMA substrates, and immunostained for lamins A-C (red) and B1 (green). Hoechst 33342 (blue) stained nuclei. (**C**) Linear regression analysis of lamins A-C/B1 ratio in glial cells in control (n= 78) and ln2PMMA (n= 792) across time in culture. Scatter plots of fitted RG probability for increasing lamins A-C/B1 ratios at (**D**) 1DIV, (**E**) 3DIV and (**F**) 7DIV. Dashed line delimits 0.5 probability. Control substrate in blue and Ln2PMMA in red, the numbers correspond to the percentage of cells with fitted probability to be RG >0.5. (**G**) Confocal images of glial cells cultured for 1-7DIV on control and ln2PMMA, immunostained for β-catenin (green) and counterstained with Hoechst 33342 (blue) to identify nuclei. (**H**) Linear regression of β-catenin Nuc/Cyto ratio over time (control n= 371; ln2PMMA n= 408). Scatter plots of fitted probabilities for increasing β-catenin Nuc/Cyto ratios at (**I**) 1DIV, (**J**) 3DIV and (**K**) 7DIV. Dashed line delimits 0.5 probability. Control substrate in blue and Ln2PMMA substrate in red, numbers correspond to the percentage of nuclei with > 0.5 probability to be RG. (**L**) Confocal images of glial cells grown for 1-7DIV on control and ln2PMMA substrates immunostained for YAP/TAZ (green) and counterstained with Hoechst 33342 (blue) to identify nuclei. (**M**) Linear regression analysis of lamins A-C/B1 ratio in glial cells in control and ln2PMMA across time in culture (control n= 274; ln2PMMA n= 346). Scale bar: 20µm, inset in G, L 10µm. Statistical analysis for linear regression ANOVA **p<0.01.

In2PMMA driven chages in lineage-specific gene expression requires mechanoelectrical calcium signaling

We tested additional mechanotransduction mechanisms that could be functionally involved in RG induction. Ca^{2+} signaling serves as a central mechanotransduction mechanism that link tension forces and nuclear morphology to transcriptional programs and cell proliferation[39]. Nuclear β-catenin and Ca^{2+} signaling interaction is involved in the differentiation of human NPC (hNPC)[40], and non selective cation-permeable mechanosensitive channels (MSCs) modulate neuronal-glial lineage choice in response to mechanical signals[41]. Findings that raised the question of whether mechanoelectrical changes might also be required for effective astrocyte to RG fate switch. Therefore, we performed a pharmacological approach to block MSCs mechanoelectrical activation and downstream Ca^{2+}-dependent signaling without afecting the mechanical loading and nuclear deformation itself. To block cationic MSCs currents we used the spider venom peptide GsMTx4 that selectively inhibits Ca^{2+} influx in response to membrane deformation[42]. To block intracellular Ca^{2+} downstream signaling we used KN93, a competitive inhibitor of Ca^{2+}/calmodulin (CaM) which binds to CaM-dependent protein kinase II (CaMKII) preventing Ca^{2+} activated gene expression[43,44]. Glial cells grown on control or In2PMMA for 3DIV were treated for 3h with GsMTx4 (1.22μM), KN93 (5 μM) or vehicle (PBS or DMSO respectively) (**Figure 4**). Consistent with our previous findings, GFAP+ astroglia was significantly lower and Pax6+ RG significantly higher in In2PMMA with respect to control substrate in vehicle-treated conditions, while these substrate-dependent differences were abrogated after 3h of GsMTx4 (**Figure 4A**) or KN93 (**Figure 4B**) tratment. In both cases, the pharmacological treatment does not block nuclear elongation in In2PMMA and therefore, the In2PMMA-induced increase in predicted RG detected with the RGM model remained mostly unchanged (RG>0.5: 0.21 in vehicle to 0.25 in GsMTx4; 0.31 in vehicle to 0.29 in KN93). Data suggesting that Ca^{2+} signaling is a downstream signaling during mechanical-driven RG induction.

RG nuclear morphology is associated with the presence of nuclear calcium waves

Somatic Ca^{2+} waves in embryonic cortical RG regulate gene expression, proliferation, neurogenesis potential, structural scaffold maintenance and neuronal migration[44,45,46,47,48,49]. Hence, we asked wether mechanically-induced RG present spontaneous somatic Ca^{2+} waves as occurs *in vivo*. We performed fluorometric calcium imaging using the Ca^{2+} indicator Oregon Green™ 488 BAPTA-1, AM (OGB), which binds free intracellular calcium in living cells. We coupled nuclear Ca^{2+} readout with our RGM model, to directly assess whether cells with RG nuclear morphology have specific somatic Ca^{2+} dynamics. After Ca^{2+} imaging, the recorded samples were fixed and

immunostained for Pax6 and nestin detection, to further correlate individual cells activity with RG marker expression (**Figure 5A-B**).

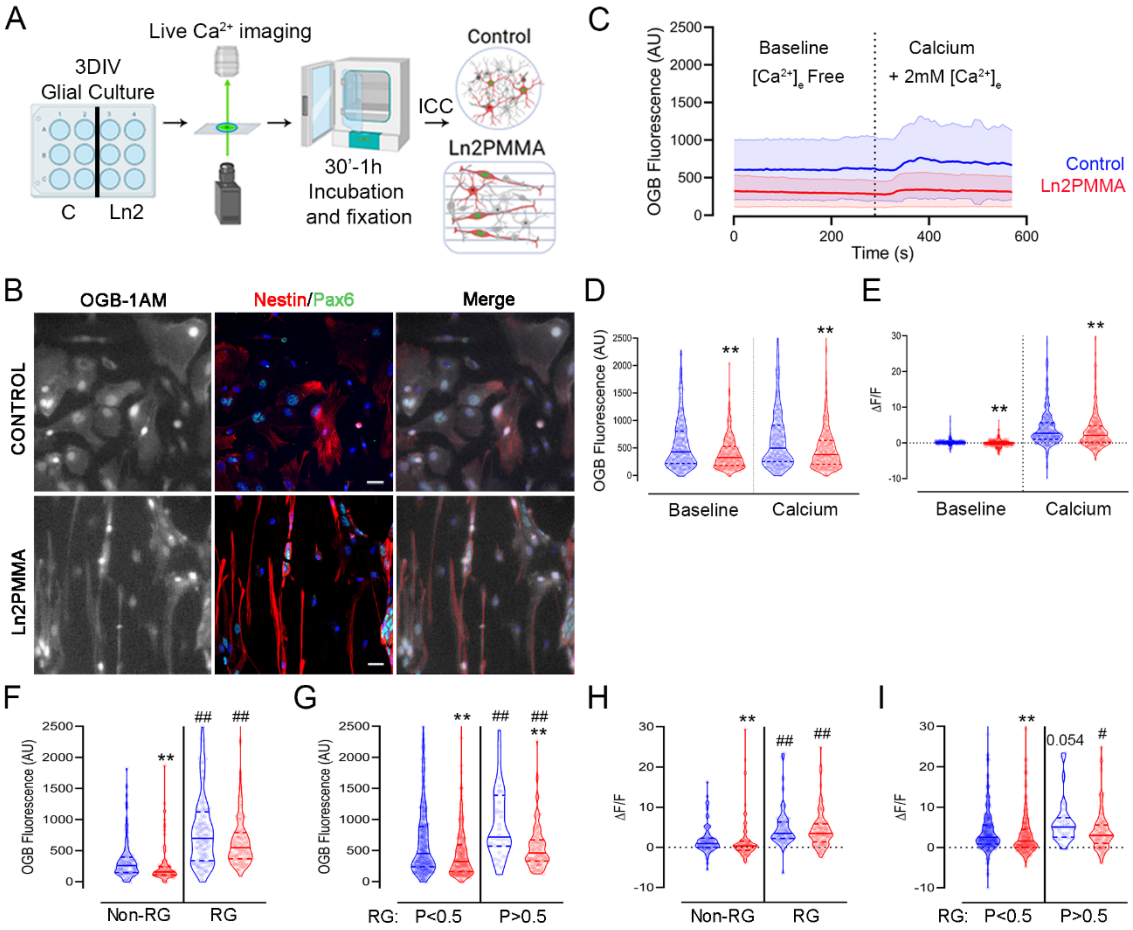

Figure 5: Evaluation of intracellular Ca^{2+} dynamics in glial cells grown on control and ln2PMMA substrates. (A) Experimental design. **(B)** microscopy images of glial cells grown for 3-4 DIV on control and ln2PMMA substrates live-loaded with OGB (white) and immunostained after fixation for RG markers Pax6 (green) and nestin (red), using Hoechst 33342 for nuclei (blue) detection. **(C)** Intracellular Ca^{+2} levels in nuclear roys were analyzed by background subtraction (F(t)-background) method and represented as signal mean +/- 95% CI (shadow area) in control (blue, n=401 cells) and ln2PMMA (red, n=399 cells) substrates. Baseline are extracellular Ca^{+2} free and calcium has 2 mM $CaCl_2$. Violin plots representing **(D)** average fluorescence intensity in each nucleus and **(E)** spontaneous nuclear Ca^{2+} transients (average ΔF/Fo), at baseline and calcium conditions in glial cells grown on control and ln2PMMA. Violin plots representing the average fluorescence intensity in each nucleus of **(F)** Pax6+ RG (control n= 98; ln2PMMA n= 133) and non-RG cells (control n=119; ln2PMMA n= 113), **(G)** RGM model predicted RG (p>0.5) and non-RG p<0.5 in calcium condition. Violin plots representing spontaneous nuclear Ca^{2+} transients in **(H)** Pax6+ RG and non-RG cells, and **(I)** RGM model predicted RG (p>0.5) and non-RG p<0.5, in calcium condition. Scale bar: 25µm. Statistical analysis: Kruskal Wallis and multiple comparison post-hoc tests. Differences between control and ln2PMMA * p<0.05, **p<0.01; differences between cell types or tratements # p<0.05, ## p<0.01. Four different samples for condition.

In general, we found more intense calcium signal in the nuclear region than in the cytoplasm (**Figure 5B**). Subsequent analysis revealed relative differences in nuclear Ca^{2+} fluorescent intensity between cells grown in control and ln2PMMA substrates (**Figure 5C**), with significantly lower Ca^{2+} signal in ln2PMMA than in control substrate, both at baseline (calcium-free extracellular medium) and in calcium conditions (2mM extracellular Ca^{2+}, for more details see methods section) (**Figure 5D**). Then, we analyzed

the presence of spontaneous nuclear Ca^{2+} oscillations (transients) by calculating the average of ΔF/Fo (basal/resting value) at baseline and calcium conditions. In general, spontaneous Ca^{2+} transients were rare at baseline and increased considerably in calcium conditions, indicating their depencence of extracellular Ca^{2+}. Consistent with their lower basal intracellular Ca^{2+}, glial cells grown on ln2PMMA had significantly less and smaller spontaneous nuclear Ca^{2+} transients, both, in absence and presence of extracellular Ca^{2+} (**Figure 5E**). When segregated by cell type, non-RG in ln2PMMA have significantly lower nuclear intracellular Ca^{2+} than in control substrate. Pax6+ RG had significantly higher nuclear intracellular Ca^{2+} than non-RG cells, and accordingly, larger calcium transients in both substrates, despite a mild reduction in ln2PMMA (**Figure 5F, H**). By applying our RGM model, we found that predicted RG ($p>0.5$) had significantly higher basal nuclear intracellular Ca^{2+} and spontaneous Ca^{2+} transients than non-RG cells, regardless of the substrate type and the presence or absence of extracellular Ca^{2+} (**Figure 5G, I**). These data specifically link the RG nuclear morphology to higher nuclear calcium dynamics, as occur in the cortical ventricular zone *in vivo*[47], and aligned with the notion that Ca^{2+} signals are rare in the astrocytic soma[46].

Conservation of RG nuclear morphology constraints across species

We constructed our RGM model using nuclear data from 2D images of glial in vitro cultures at different cell densities, intentionally excluding highly confluent zones where the lack of space and cell-contact inhibition drives glial cells out of the cell cycle and promotes astroglia differentiation. This design choice limits the applicability of the RGM model in such conditions, where it could still be applied but preventing extrapolation. On the other hand, the LogOdds ratio function is only based on nuclear morphology parameters, as all terms related to cell density restrictions were removed. Therefore, it can be applied to highly confluent cell cultures or even brain tissue sections. To showcase its capabilities, we used the LogOdds ratio function at F(0) threshold, restricted to the nuclear area range of Pax6+ cells, as an initial approach to inquire inter-species conservation of RG cells' nuclear morphology *in vivo* and *in vitro*.

Using cortical sections of embryonic day 18 (E18) mice, we analyzed the nuclear morphology of cells located in the ventricular zone (VZ; mostly populated by Pax6+ RG), cells located in the subventricular zone (SVZ; mostly populated by intermediate progenitors), and cells in the intermediate zone (IZ; at this age mainly occupied by migrating neurons). Consequent with the region-specific cellular distribution, we found that the percentage of nuclei within the RG nuclear zone were 80.9% in the VZ, 20.4%

in the SVZ, and 10.2% in the IZ (**Figure 6A**). These results closely resemble our *in vitro* data and support the notion that RG nuclear constraints are present *in vivo*.

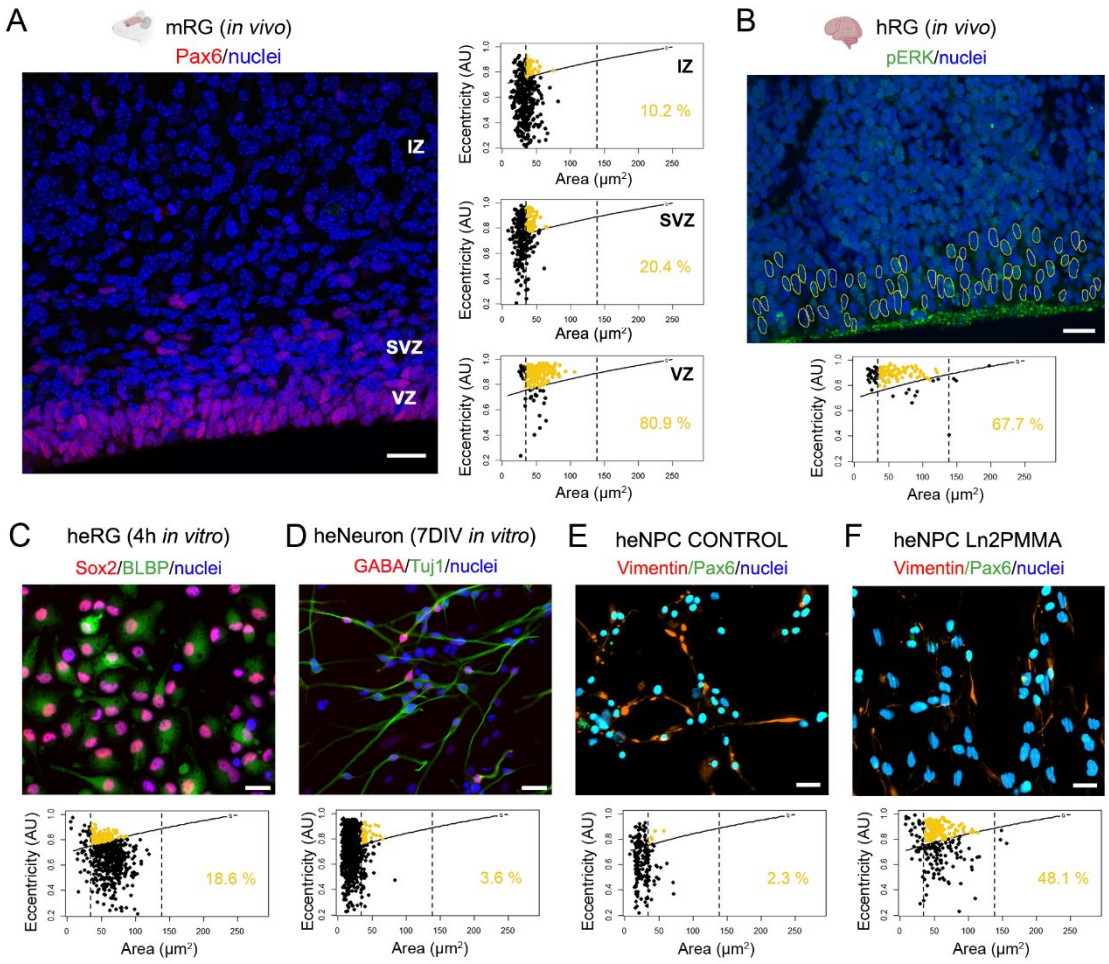

Figure 6: Conservation of RG nuclear morphology between mice and human. Microscopy images and corresponding surface plots representing the LogOdds ratio function at F(0). Yellow dots and percentages correspond to the nuclei fitting into the RG nuclear zone stablished by our RGM model. **(A)** Coronal section of the mouse cerebral cortex at embryonic day 18 (E18) immunostained for Pax6 and Hoechst 33342 for nuclei (blue) detection. **(B)** Coronal section of fetal human cerebral cortex at gestational week 10 (GW10) immunostained with pERK (green, highlighted nuclei) and using DAPI to label nuclei (blue). **(C)** hRG culture obtained from the embryonic brain shown in **(B)** and cultured for 4h in a flat control substrate immunostained for Sox2 (red) and BLBP (green), and using DAPI to label nuclei (blue). **(D)** 7DIV hneurons differentiated form hRG in **(C)** immunostained for GABA (red) and Tuj1 (green), and using DAPI to label nuclei (blue). HeNPC grown on control substrate (Matrigel coated) **(E)** and Ln2PMMA **(F)**, immunostained for Vimentin (red) and Pax6 (green) using Hoechst 33342 for nuclei (blue) detection. In each panel, the surface plots in function of area (x-axis) and eccentricity (y-axis) represent the LogOdds ratio function at F(0), with vertical dashed lines delimitating the nuclear area range of Pax6+ cells in mouse glial cultures (Amin=34.75µm2 / Amax=139µm2). Scale bar: 20µm. VZ: ventricular zone; SVZ: subventricular zone; IZ, intermediate zone.

To inquire whether similar nuclear morphology constraints were present across species, we analyzed histological sections from fetal mouse and human brains, as well as *in vitro* RG cultures derived from 10-15 gestional week human fetuses (material derived from[50,51]). In the human embryonic cortical sections, human RG (hRG) nuclei were identified by its location in the VZ and pERK expression, as ERK signaling is required for

RG maintenance[52]. Consistently with our findings in mouse, 67.7% of putative hRG nuclei in the VZ fitted into the model defined RG nuclear zone (**Figure 6B**), supporting the evolutive conservation of the nuclear constraints identified with our RGM model.

To evaluate whether tissue dissociation-induced loose of basal and apical anchorage and further grown and differentiation in culture impact nuclear morphology, we analyzed primary cultures of hRG obtained from cortical dissections of midgestation fetal brains. Immunomagnetic cell sorting allowed purification of hRG which were cultured and imaged at 4h and after 7DIV, to track their differentiation into neurons[50,51,53]. Culture hRG for 4h *in vitro* in standard poly-D-lysine (PDL) coated flat substrate induced a rapid exit from the model defined RG nuclear zone, passing from 67.7% to 18.6% of nuclei (**Figure 6C**). Moreover, after 7DIV only a residual 3.6% nuclei fitted within the RG nuclear zone, indicating that hRG-derived neurons have a clearly different nuclear morphology (**Figure 6D**). We next tested if ln2PMMA substrate anisotropy favors the acquisition of potential nuclear morphologies in neural cells at early stages of differentiation. In these experimentes, we utilized human stem cell-derived NPCs (hNPCs; for more details see methods section). We found that only 2.3% of hNPC nuclei fell within the RG nuclear zone when cultured in control PDL substrates (**Figure 6E**), while in ln2PMMA, nearly 50% of hNPC nuclei fitted in the RG nuclear zone (**Figure 6F**). Altogether, our data indicate that the anisotropic topology of the embryonic RG niche imposes RG nuclear morphology constraints that are conserved between mouse and human through evolution, and that RG/NSC fate can be dynamically modulated by mechanical signals within de niche.

Discussion

We have previously demostrated that primary astrocytes cultured on ln2PMMA, a non biodegradable micro 3D substrate that mimicks the mechanical anisotropy and surface properties of the embryonic RG niche, adopt a bipolar shape aligned with the topography, express Pax6 and adquire a funcional RG fate that supports neuronal migration[14,15]. In order to decipher the mechanobiological effectors associated to this phenomenon, we developed a multivariate generalized linear model for RG identification (named RGM model) that takes into account nuclear morphology and the structural anisotropy of the embryonic RG niche. We demonstrated that the lineary oriented mechanical signals from ln2PMMA force the astroglial cell nucleus to elongate and adopt an RG-specific morphology, wich is restricted to a defined RG nuclear zone within the LogOdds ration function. The adquisition of RG nuclear morphology is associated to the presence of somatic Ca^{2+} transients, which are relevant for RG proliferation and differentiation[23,47].

RG nuclear morphology is conserved *in vivo/in vitro* as well as between mice and human, pointing to the structural anisotropy of the niche as a key factor for maintaining/inducing RG fate and functionality. Our studies in mouse and human underscore that standard culture on flat isotropic substrates disrupt the polarized mechanical signals of the embryonic neurogenic niche, altering neural cells' nuclear morphology and functionality. Therefore, the use of anisotropic RG-mimetic micro3D substrates, like In2PMMA, will serve as a better platform for the estudy of early neurodevelopmental proceses *in vitro,* improving the stemness, functionality and developmental potential of cultured hRG and hNPC.

One of the principal challenges in classifying neural cells types and states is their inherent heterogeneity and lack of specific markers. Clasification complexity raises during developmental transitions, with lineage markers often shared among different cell types[54,55,56,57]. For instance, Sox2 is considered a general stem cell marker and Pax6 a cortical RG marker, but both are also expressed in specific astrocytic and neuronal subsets. Similarly, nestin is expressed in RG but also in immature and reactive astrocytes as well as in mesenchymal stem cells, while the widely used astrocytic marker GFAP is also expressed in NSC and ependymal cells. To overcome the lack of lineage specific markers and immunolabeling drowbacks, image-based computational deep neural networks and machine learning approaches have been developed, allowing the assessment or identification of cell types and states based in cell and nuclear morphological parameters[58,59,60,61]. Despite they can reach impressive performance levels based in cellular structures and bright field images, as in predicting neural stem cells differentiation[62], they fail to identify the relevant parameters for system classification or to give clues for further model improvement. Our multivariate generalized linear RGM model provides a novel classification tool for RG fate prediction, based on known specific 2D nuclear morphology parameters that retain biological interpretability. The accuracy of the RGM model in identifying RG cells, irrespective of the culture substrate, unveils the existence of intrinsic mechanical factors within the cells that constrain the range of possible nuclear shapes in functional RG progenitors. The current RGM model construction imposes restrictions to their use in high cell density conditions as *in vivo.* Nevertheless, the use of LogOdds ratio function as an initial *in vivo* approach, have revealed that nuclear morphology constraits are evolutionary conserved in RG. This supports the utility of biologically interpretable generalized linear models like ours. The RGM model can be further improved for a broader and more precise stratification of cell types and states in different species, *in vivo* and *in vitro.* For instance, by increasing the cell-density range of use, correcting for cycling cells, and adding additional 3D nuclear

parametters, as volume or rugosity. By integrating multimodal data with known nuclear morphology parameters, our RGM model can evolve in a valuable tool for RG identification and cell state characterization in different developmental paradigms in human and model organisms.

From the mechanistic poin of view, it is well known that RG to astrocyte differentiation is bidirectional[9], that astrocyte to RG/NSC transition can occur after a brain trauma[10,11,63], and that can be induced by RG biomimetic materials *in vitro*[14,15] and *in vivo*[64]. Despite much work has been done in understanding the molecular mechanisms regulating RG diferentiation[3,34,65,66], the mechanotrasduction mechanisms implicated remain pooly understood. Due to its micro 3D topography, non-biodegradability and their use uncoated, In2PMMA mechanical signals remain stable trough time in culture, making it a good platform for mechanotransduction studies. Mechanistically, we have demonstrated that In2PMMA induces the elongation of astrocyte soma and nucleus, morphological changes that lower nuclear lamins A-C/B1 ratio from the day of seeding and before significant changes in the expression of RG molecular markers. This temporal sequence aligns with recent studies on the dynamics of mechanosensitive NSC differentiation indicating that lineage commitment occurs within the 2-3 days after initial adhesion[67]. Nuclear β-catenin signaling as emerged as one possible mecanotransduction mechanism involved in RG induction, as β-catenin binding to Pax6 promoter induce its transcription, and their crossed interaction is required for RG self-renewal/differentiation balance[34,38,68]. Therefore it is whorth considering that the sustained nuclear β-catenin observed in In2PMMA might transcriptionally upregulate Pax6 expression, wich might further sustain nuclear β-catenin signaling, inducing RG fate.

Aside for In2PMMA-induced mechanical deformation, our resuts indicate that the switch in the expression of astrocyte to RG molecular markers also requires sustained mechanoelectrical changes. Changes probably involving Ca^{2+} influx through cationic MSCs and nuclear Ca^{2+} signaling, as pharmacological inhibition of MSCs function and CAMKII activity for 3h, abolish substrate-induced gene expression differences. Consistently, RG-specific nuclear shape is associated with higher somatic/nuclear resting Ca^{2+} and Ca^{2+} transients than the observed in non-RG cells, paralleling the Ca^{2+} waves described in RG *in vivo*[47]. Based on our data, we can hypothesize a bimodal biomechanical/bioelectrical mechanism for astrocyte to RG transitions in response to mechanical signals. We can speculate that cellular/nuclear deformation might induce persistent chages in the activation state of MSCs, which together whith changes in nuclear lamin composition and chromatin organization will mediate Ca^{2+}-driven

expression of cell type-specific genes. Although much more mechanistic work will be required to prove this hypothesis.

Conclusions

This study underscores the critical role of nuclear morphology and mechanosensitive signaling in RG fate acquisition and functional identification. Using the anisotropic ln2PMMA substrate as a model system, we demonstrated that mechanical cues rapidly shape nuclear morphology, preceding the expression of RG-specific molecular markers. Our RGM model, developed from these observations, effectively predicts RG probability based on nuclear morphology parameters, providing a robust classification tool for identifying functional RG *in vitro*.

Thus, this work provides a framework for studying the interplay between nuclear mechanics, morphology, and cell fate decisions, offering a novel approach for RG identification and differentiation studies. Future research should focus on refining anisotropic culture systems, exploring the influence of mechanical signals on other neural cell lineages, and elucidating the molecular mechanisms driving nuclear deformation and RG fate commitment. Additionally, integrating computational tools to model and analyze the complex interactions between mechanical and molecular cues could provide deeper insights, with potential applications in regenerative medicine and developmental biology.

Author's contributions: Conceptualization: SA, JPS, JA, CB. Design of the work SA, JPS. Experiments: JPS (mouse related experiments), JAO (human related experiments). Image acquisition and processing: JPS. Calcium experiments: RS, JPS. Software development for image and calcium analysis: CB. Data processing: JPS. Data analysis: JPS, SA. Statistical model generation: JA, JPS. Single-cell transcriptomics metanalysis: LG. Supervision SA, JA, CB. Original draft preparation SA. JPS. Writing rewiew and editing all authors. All authors read and aprobed the final manuscript.

Funding: This work was supported by the grant PID2020-115748RB-I00 from Spanish Ministry of Science and Innovation (MICINN) to SA. PID2023-150234NB-I00, and Gobierno de Aragón under Research Group E46_23R: Modelos Estocásticos to JA. We are also grateful to funding sources PID2020-114407RA-I00 and CNS2023-144820 (JAO) funded by MICIU/AEI/10.13039/501100011033 and by European Union NextGenerationEU/PRTR. Researchers also thank Programme/Generalitat de

Catalunya (2021 SGR 00344) (SA and JAO), the Ramon y Cajal fellowship RYC2019-026980-I (JAO), and Maria de Maeztu Units of Excellence: Institute of Neurosciences, University of Barcelona (JAO and SA).

Data availability statement: All study data are included in the article and/or supplementary data and in the https://github.com/PepPau/RGM-model-main-scripts.git. Original data will be available upon request when this article will be published.

Acknowledgements: We also thank the Biologia-Bellvitge Unit from Scientific and Technological Centers (CCiTUB), Universitat de Barcelona, and Benjamin Torrejón for their support and advice on confocal microscopy technique, and Marta Cuenca and Cristina Martinez for their technical support in preparing human NPC cultures on control and In2PMMA substrates.

Conflicts of interest: The authors declare no competing or finantial interest.

STAR Methods

Animals and cell cultures

The Ethical Committee for Animal Experimentation of the University of Barcelona and the Generalitat de Catalunya with order nº: 9656 approved animal housing and all experimental procedures in accordance with Spanish and EU regulations.

Cortical primary cultures

Cortical glial cells were obtained from newborn (P0-P1) Swiss albino mice of both sexes. Briefly, after brain extraction, cerebral cortices were dissected out free of meninges in dissection buffer (PBS + 0.6% of glucose (Sigma), 0.3% bovine serum albumin (BSA) (Sigma)) and digested with 5 ml of trypsin (Life Technologies) with 500µl of DNAse I (Sigma) for 10 minutes at 37º. The tissue was mechanically dissociated in growing medium (GM) Dulbecco's Modified Eagle Medium (DMEM, Biological Industries), 10% normal horse serum (NHS, GIBCO), 1% penicillin-streptomycin (P/S, Biological Industries) and 1% L-glutamine (Biological Industries). After centrifugation and resuspension, passage 0 (Ps0) cells were plated in flasks and grown for 14 days. To remove contaminating microglial and oligodendroglia progenitor cells, cultures were shaken overnight at 37ºC followed by a change of medium the day before starting the experiment (adapted from[69]). For all experiments, adherent Ps0 glial cells were dissociated with trypsin, counted, and plated on the different substrates (borosilicate glass coverslips or Ln2PMMA) at a density of 2-4x10^4 cells/cm^2 in 24 wells and grown for 1-14 DIV in Neurobasal™ (NB, Gibco), 3% NHS, 1% P/S and 1% L-glutamine (experimental medium, EM) (Ps1). As substrates are are hydrophobic and uncoated, we first carefully spread the drop with cells (60µl) onto their respective surfaces and left 20-30 minutes at 37ºC in the incubator to favor cell adhesion[69]. Then each well was filled with the remaining medium required (440µl).

Human induced pluripotent stem cells (iPSCs)

Human induced pluripotent stem cell (iPSCs) line 18a and embryonic stem cell (ESC) line HUES 64 (Harvard Stem Cell Institute) were cultured in mTeSR medium on Matrigel-coated plates (ThermoFisher BD354277). Cell lines were transferred to University of Barcelona-IDIBELL after Generalitat de Catalunya Health Department's approval and material transfer agreement (MTA) stablished between Institutions (Signed by Ortega JA as principal investigator). The cells were fed with fresh mTeSR medium daily (Stem Cell Technologies - 85850). For thawing or splitting, iPSCs were resuspended in DMEM/F-12 media (FISHER SCIENTIFIC, Gibco, 11574546) and cultured in mTeSR

supplemented with 10 μM ROCK inhibitor (RI) (Bio-Techne, ToCris, #1254) for 24-48 hours. Basic passaging was performed using EDTA (0.5 mM), while accutase (Innovative Cell Technologies - AT 104-500) was used for human neural progenitor cells (hNPCs).

Human neural progenitor cells (hNPCs)

Human neural progenitor cells (hNPCs) were derived from the human iPSC or ESC following the protocol previously described by (Topol et al., 2015). Briefly, iPSCs were dissociated with accutase (Sigma-Aldrich) and replated in matrigel-coated plates and mTESR media with RI, to obtained a 70% confluency by the following day (day 0), when mTESR was replaced by N2/B27 media [DMEM/F-12 with 1X N-2 (100X, 12013479, Gibco), 1X B27™ (50X, 11530536, Gibco), and 20ng/ml of recombinant human FGF-basic – (PHG0264, Fisher Scientific)] supplemented with dual SMAD inhibitors (0.1M LDN193189 and 10M SB431542) for 6 days. Media was changed on a daily-base, and from day 7, we also incorporated 1 μg/ml laminin (from day 7) to the media. By day 12 neural rosettes were dissociated utilizing STEMdiff™ Neural Rosette Selection Reagent (StemCell Technologies, #05832). The dissociated NPC were resuspended and replated in matrigel-coated plates or In2PMMA with NPC media (DMEM/F-12 supplemented with N2 and B27).

Fetal tissue samples and human RG cultures

Fetal tissue samples were obtained and utilized at Zecevic's laboratory (University of Connecticut Health Center). Samples were originally sourced from Advanced Bioscience Resources (ABR) and Human Developmental Biology Resource (HDBR), after parental written consent and approval from the Ethics Committees of the participating Institutions[50,51]. Human materials were handled with special care and following all necessary requirements and regulations set by the Ethics Committee of the University of Connecticut and the Helsinki Declaration. Samples were transferred to University of Barcelona-IDIBELL after UB-Bioethic Committee approval and MTA stablished between Institutions (Signed by Ortega JA as principal investigator). The fetal brains used in the study exhibited no signs of disease or abnormalities upon thorough neuropathological examinations. The developmental stage was determined based on gestational weeks after conception and ultrasound findings. The tissue was collected in oxygenated Hank's balanced salt solution (Invitrogen) and transported on ice. After dissection, cortical tissue was mechanically and enzymatically dissociated using 0.025% trypsin-EDTA (Invitrogen) and DNAse I (2 mg/mL, Sigma-Aldrich). The resulting cells were cultured in poly-D-lysine (Sigma-Aldrich) coated flasks containing proliferation medium (PM), consisting of DMEM/F12 (Invitrogen), B27 supplement (Invitrogen), basic fibroblast

growth factor (bFGF; 10 ng/mL, Peprotech), epidermal growth factor (EGF; 10 ng/mL, Millipore), and penicillin/streptomycin (Invitrogen). After cell expansion, we utilized MACS® Technology to immunomagnetically sort human RGCs from fetal brain derived cultures with anti-CD15-antibody-coated microbeads (Miltenyi Biotech). Detailed description of the protocol followed is described in[50,51]. Human RG were cultured on poly-D-lysine-coated and grown with PM for expansion for 1-3 days. For differentiation purposes, bFGF and EGF was removed from culture media.

For immunocytochemistry of human RG cultures, cells were fixed with 4% paraformaldehyde for 30 minutes, blocked for 1 h in PBS with 0.1% normal goat serum (Gibco) and 0.1% Triton (Sigma-Aldrich), and incubated cells overnight at 4 °C with the primary antibodies Sox2 (Santa Cruz biotechnologies, sc-17320) and BLBP (Abcam, ab27171) for RGC identification; and GABA (Sigma, WH0026468M1) and TUJ1 (Dako, PRB-435P) for neuron identification. Next day, cells were incubated for 1h with the Alexa488- or Alexa555-conjugated secondary antibodies (1:500, Molecular Probes). Cell nuclei were counterstained with bisbenzimide (Hoechst 33342) (Sigma-Aldrich).

For immunohistochemistry, fetal forebrain blocks were fixed in 4% paraformaldehyde overnight, cryoprotected in PBS + 30% sucrose, and TissueTek OCT blocks were made by freezing in liquid nitrogen for subsequent sectioning 15-µm sections). Sections were blocked in Tris-NaCl-Tween buffer (TNT) [0.1 M, pH7.5 Tris-HCl (Thermo Fisher Scientific); 0.15 M NaCl (Thermo Fisher Scientific); and 0.05% Tween] with 0.5% blocking reagent (Roche) and incubated overnight at 4 °C with primary antibodies. Next day, sections were incubated with Alexa555 or Alexa 488 (Molecular Probes)-conjugated secondary antibodies and then briefly with bisbenzimide (Sigma-Aldrich) for nuclear counterstaining.

PMMA micropatterning, characterization and sterilization

Goodfellow Ltd. (UK) supplied PMMA sheets (125 µm thick). The Nanolithography Laboratory of the Institute of Microelectronics of Barcelona (IMB) - National Center of Microelectronics (CNM) CSIC prepared Ln2PMMA substrates as a service. Micropatterning consist in linear grooves of 1µm deep/tall and 2µm wide, introduced by nano-imprinting lithography (NIL) and characterized as previously described[14,70]. For cell culture, Ln2PMMA substrates were cut to fit in 24 multi-well culture plates, sonicated for 10 minutes in sterile water, sterilized in 70% ethanol for 15-20 min, rinsed with sterile water for 20 min, left dry and then used uncoated. We used borosilicate glass cover slips as control substrates, since there were no major differences in cell morphology and

expression of differentiation markers between no patterned PMMA, glass and culture plastic[14].

Immunofluorescence

Cells were fixed in 4% PFA in 0,1M phosphate buffer (pH of 7.2) for 20'. Then, samples were transferred to a new multi-well plate, washed with PBS (5' x 4), and blocked for 2h using phosphate buffered saline (PBS) with 3% normal serum (horse and/or goat, Gibco), 0.05% Triton (Sigma-Aldrich), and 0.2M glycine. Samples were then washed with PBST (PBS + 0.05% triton, 5' x 3) and incubated with primary antibodies overnight at 4ºC with incubation buffer (PBST + 1% normal serum). The next day, samples were washed with PBST (5' x 4) and incubated for 2h at room temperature in their appropriate anti-mouse, anti-rabbit or anti-goat Alexa488, Alexa555, or Alexa 649-conjugated secondary antibody (1:1000, Life Technologies). After washing with PBST (5' x 2), samples were incubated 15' with Hoechst 33342 (1 µl/mL, life technologies, 1:20000) in PBS to counterstain cell nuclei. Lastly, samples were washed with PBS, (5' x 3) and mounted with in-house Mowiol preparation (Calbiochem, standard protocol). Used antibodies and dilutions are listed in the table below.

Primary antibody	**Dilution**	**Reference**	**Molecule and Cell type marker**
Rabbit anti glial fibrillary acidic protein (GFAP)	1:3000	DakoCytomation - Z0334	Intermediate filament, mature astrocyte marker
Rabbit anti NG2	1:600	Millipore - AB5320	Proteoglycan, OPC marker
Rabbit anti Pax6	1:500	Abcam - ab195045	Transcription factor, RG marker
Mouse anti Pax6	1: 500	Santa Cruz - sc-81649	Transcription factor, RG marker
Rabbit anti Sox2	1:3000	Abcam - ab97959	Transcription factor, general stem cell marker
Rabbit anti GSX2	1:500	Thermofisher - 15504202	Transcription factor, Tripotential intermediate progenitor
Mouse anti Nestin	1:3500	BD Pharmigen - 556309	Intermediate filament, RG / immature astrocyte marker
Rabbit anti Ki67	1:500	Abcam – ab15580	No-histone protein, cell cycle marker.
Rabbit anti PH3	1:500	Millipore - 6570	Histone protein, mitosis marker.
Mouse anti Lamin A/C	1:3000	Invitrogen – 14-9847-82	Ubiquitous, nuclear lamina
Rabbit anti Lamin B1	1:3000	Abcam - ab16048	Ubiquitous, nuclear lamina

Rabbit anti YAP/TAZ	1:1000	Cell Signaling - 8418	Transcription factor, ubiquitous, transcription factor
Rabbit anti β-Catenin	1:3000	Abgent – AX10009	Key downstream component (protein) of the canonical Wnt signaling pathway.
Rabbit anti β-Catenin	1:3000	Abgent – AX10009	Key downstream component (protein) of the canonical Wnt signaling pathway.

Image processing and cell nuclei segmentation

For image acquisition, we used an LSM 880 spectral confocal microscope (Carl Zeiss, Germany) and LD LCI Plan-Apochromat 25x/0.8 Imm Korr DIC M27 and Plan-Apochromat 40x/1.3 Oil DIC UV-IR M27 objectives (Images were mounted with the ZEN (blue edition) software to obtain projections. We adjusted the number of optical confocal sections depending on the experiment and markers. For each marker, the same settings for acquisition and projection were used for all the experiments. A range of six to nine images from two to four different samples were used for each study. Images were randomly taken at different sample areas while avoiding those of high cell confluence (middle of the sample). In these areas, intercellular interactions overcome mechanical signals from In2PMMA substrate and cells tend to differentiate into astrocytes, as in control substrate[15].

We employed a custom-designed, high-throughput image analysis algorithm developed in MATLAB to extract cellular and nuclear parameters from each image. This allowed us to simultaneous correlate lineage markers with nuclear morphology at the single-cell level. Nuclei segmentation was performed in z-stack orthogonal maximum projections (cell-lineage assignments) or from average projection (intensity fluorescence assays), as we found no significant differences between both types of analysis (**Figure S4**).

Our custom-designed algorithm allowed for semiautomatic processing of immunofluorescence images through the application of specific functions for each wavelength channel. These functions implement advanced segmentation methods combining simple thresholding with more refined techniques such as a modified version of the top-hat algorithm[71]. Segmented pixels in the blue channel (Hoechst staining) were used for the extraction of the nucleus perimeter, area, and eccentricity. Eccentricity (E) is the ratio of the distance between the foci of the ellipse that has the same second-moments as the region (nucleus) and its major axis length. It is a non-dimensional measure that indicates the range of nuclear shape from circular (E=0) to a linear segment

(*E*=1) shape. Total nuclei per image was also considered to detect correlations between cell density with their morphological features.

When a nucleus is segmented, the algorithm extracts the total intensity within the nuclear region, as well as within the surrounding (perinuclear) region that has the same area as the original nucleus, as proposed[31] for the analysis of cytosolic to nuclear protein translocation. We used this approach to calculate nuclear and cytoplasmic intensity ratios in transcriptional cofactors analysis (YAP/TAZ and β-catenin) (**Figure S5A**) and nuclear fluorescence intensity of lamin A-C and lamin B1 nuclear proteins (**Figure S5B**). Intensity extraction from two different markers within the same nucleus required specific attention to avoid fluorescence overlapping and the use of the same segmentation in both channels. This step was manually performed and revised.

Figure S6 illustrates the nuclei analysis app developed for the image analysis with examples of the main features used. We included different microscopes to the MATLAB algorithm to be able to combine data from different sources (**Table S3**).

To optimize nuclear detection, we evaluated various nuclear staining methods to identify the one that maximized the number of detectable nuclei under the program's default parameters, avoiding time-intensive parameter adjustments. Lamin B1, a nuclear intermediate filament commonly used in nuclear morphology studies[72], was compared to Hoechst staining, a frequently used nuclear counterstain in immunostaining protocols (**Figure S7A**). Our results showed that Hoechst staining facilitated the segmentation of 16% more nuclei than lamin B1 in control samples, and 18% more in In2PMMA substrates, based on a reference detection rate of 50% (**Figure S7B**). Importantly, there were no significant differences in area or eccentricity measurements for individual nuclei between the two staining methods (**Figure S7C**). Therefore, Hoechst was selected as the primary nuclear stain for all segmentation analyses.

Nuclear morphology data from in vivo images was obtained using the freehand tool of ImageJ Fiji Software. For analysis, individual images were selected, ranging from a single slice to a maximum projection of three consecutive slices from the image stack. Cell density associated to in vivo images was manually calculated and assigned per zone instead of per picture.

Generalized linear model construction for RG markers

Model Overview

To investigate the relationship between nuclear morphology parameters and the expression of radial glia (RG) cell markers, we constructed a Generalized Linear Model

(GLM) in R (R Core Team, Vienna, Austria), a statistical computing environment. The model analyzes data obtained from confocal images of primary mouse cortical astrocyte cultures grown for 3 days in vitro (3DIV) on either control or In2PMMA substrates, with cells immunostained using specific markers as previously described.

Image Variable Definition

For model inputs, we defined a covariate vector comprising:

- Nuclear morphology parameters: Area (μm², as a measure of size) and eccentricity (dimensionless, as a measure of shape).
- Cell density: Calculated as the total nuclei count per area of the confocal image.
- Substrate type: control or In2PMMA.

The dataset was obtained from 15 independent immunofluorescence assays on glial cells cultured on both substrate types, producing a sample of 3,855 nuclei. To account for cell density variability, we captured 7-12 images per substrate condition from areas representing low, medium, and high confluence levels.

Response Variable Definition

The binary response variable classifies nuclei as RG or Non-RG based on the presence of RG markers, which vary according to cell lineage stages. A nucleus was labeled as RG if it expressed Pax6+, either alone or combined with nestin+/-, GFAP+/-, or Sox2+/-, or if it expressed Sox2+ combined with nestin+. Non-RG cells were defined as those either double-negative for Pax6/nestin, Pax6/GFAP, or Sox2/nestin, or positive for lineage-committed markers (e.g., NG2+, Gsx2+, or Pax6-/GFAP+). Cells lacking specific marker expression were labeled as undetermined cells. Markers combination and its category are listed below.

RG N=374	**Non-RG N=786**	**Undetermined N=1295**
Pax6+/Nestin+	Pax6-/Nestin-	Nestin-/Sox2+
Pax6+/Nestin-	Pax6-/GFAP+	Pax6-/Sox2+
Pax6+/Sox2+	Pax6-/Sox2-	Nestin+/--
Pax6+/Sox2-	Nestin-/Sox2-	Sox2+/--
Nestin+/Sox2+	Nestin-/NG2+	GFAP+/--
Pax6+/GFAP+	Nestin+/NG2+	Nestin+/NG2-

Pax6+/GFAP-	Nestin-/GFAP-	Nestin+/GFAP+
Pax6+/--	Nestin-/GFAP+	Nestin+/GFAP-
	Pax6-/GFAP-	Nestin+/Sox2-
	NG2+/--	Nestin+/Pax6-
	Gsx2+/--	

Model construction

We implemented a generalized linear model with a logit link to accommodate non-normal data and to predict the probability of RG marker expression based on morphological parameters. The logit function transforms the linear predictor (a weighted sum of predictor variables) into the probability of a binary outcome.

The linear prediction equation for RG (response *y* = 1) given the morphological predictor – eccentricity (*E*), area (*A*), and cell density (*D*) – is defined as follows:

$$P(RG) = \frac{\exp(\beta_0 + \boldsymbol{g}(\boldsymbol{E}, \boldsymbol{A}, \boldsymbol{D}))}{1 + exp(\beta_0 + \boldsymbol{g}(\boldsymbol{E}, \boldsymbol{A}, \boldsymbol{D}))}$$

Due to the nature of our data and the type of response, we used the function logit link to define the relationship between the linear and the expected value of the response variable. The logit link function maps the linear predictor to the odds of success in binomial distributions, as shown in the following equation:

$$logit\big(P(RG)\big) = \beta_0 + \boldsymbol{g}(\boldsymbol{E}, \boldsymbol{A}, \boldsymbol{D}) = \beta_0 + (\mathrm{poly}(\mathbf{E}, \mathrm{k_E}) + \mathrm{poly}(\mathbf{A}, \mathrm{k_A})) * (\mathbf{Material} + \mathbf{D})$$

Where *g(E, A, D)* represents polynomial expansions and interaction terms and *K* terms representing the polynomial degree.

Selected model

The model selection process was based on maximum likelihood estimation (MLE) and minimized Akaike Information Criterion (AIC) for model fit and complexity balance. Terms significant at the $p < 0.05$ level were retained in the final model. Most non-significant terms were eliminated; however, terms relevant only in specific substrate interactions were retained, even if they were non-significant in the counterpart substrate. The following table summarizes the model coefficients, standard errors, z-values, and p-values.

Term	Estimate	Std. Error	z value	p-value
(Intercept)	-5.82E+03	7.62E+02	-7.634	0

Ln2PMMA	-9.45E+02	5.66E+02	-1.669	0.095
Area	1.51E+02	2.58E+01	5.829	0
Area^2	-1.05E+00	2.22E-01	-4.755	0
Area^3	1.81E-03	5.49E-04	3.296	0.001
Control * Eccentricity^3	-2.31E+02	8.84E+02	-0.261	0.794
Ln2PMMA * Eccentricity^3	2.57E+03	7.32E+02	3.509	0
Ln2PMMA * Area	-7.33E+00	4.74E+00	-1.546	0.122
Eccentricity^2 * cell density	5.15E+00	2.49E+00	2.068	0.039
Eccentricity^3 * cell density^2	-2.75E-03	1.50E-03	-1.834	0.067
Area * cell density	-1.46E-01	4.13E-02	-3.522	0
Area * cell density^2	8.80E-05	2.37E-05	3.722	0
Area^2 * cell density	8.91E-04	2.78E-04	3.2	0.001
Area^2 * cell density^2	-6.22E-07	1.84E-07	-3.384	0.001

Substrate-specific terms allow for distinct RG classifications by substrate type (control and ln2PMMA), introducing different interaction pathways. The two primary logit equations are **eq.1** for control and **eq.2** for ln2PMMA.

The expression *logit (…)* indicated the application of the linear predictor to the associated probability to the response $y=1$, using the variables X in control or ln2PMMA. β corresponds to estimated coefficients, A corresponds to area, E to eccentricity and D to cell density. Specific terms depending on substrate were indicated as C for control and Ln2 for ln2PMMA.

Quadratic and cubic terms reflect complex relationships among nuclear morphology features and RG marker expression, with the direction and significance of each effect indicated by the z-value and p-value. We guided the model by a stepwise model selection and refinement based on AIC, ensuring model parsimony without compromising essential predictive interactions. To assess classification performance, we computed the AUC for Receiver Operating Characteristic (ROC) curves (**Figure 2** Main text).

Equation description

To identify substrate-conditioned variables, we calculated the odds ratio based on equations (1) and (2). The odds ratio serves as a measure of association between conditions or variables, allowing us to compare the impact of substrates on nuclear morphology. The odds ratio for substrates is calculated as follows:

$$Odds\ ratio = \frac{Odds\ (Ln2PMMA)}{Odds\ (Control)} = \frac{\exp(\beta_{0Ln2} + \beta_{E^3Ln2}\mathrm{E}^3 + \beta_{ALn2}A)}{\exp(\beta_{E^3C}\mathrm{E}^3)}$$

For streamlined interpretation and application, we converted this to the *log-odds ratio*. This transformation allowed us to address two critical questions:

1. Quantifying substrate effects: We determined the proportion of change in nuclear morphology driven by ln2PMMA compared to control conditions.
2. Threshold determination: At a log-odds ratio of 0, the threshold for substrate-induced versus intrinsic nuclear deformation is established, delineating an intrinsic mechanical property threshold essential for RG morphology in glial nuclei.

The log-odds ratio calculation was applied directly to nuclear data.

Model Validation Procedure

Model validation was conducted using independent datasets from glial cells cultured for 3DIV in two biological samples and immunostained for RG markers (nestin/GFAP and Pax6/nestin). The model-predicted counts of RG cells were compared to experimentally observed counts.

Dataset requirements and model application workflow

Before applying the model, new data were assessed to ensure they fell within the established parameter range of the training data. Any extrapolated data points outside this range were flagged and excluded to maintain model reliability.

The model application process included two main approaches:

1. Prediction of RG Cell Percentages: For each nucleus, fitted probabilities (0 to 1 on the x-axis) were generated and represented in density plots. Percentages of nucleus with fitted probability is over thresholds 1/2 (50%) were calculated to evaluate predictive accuracy. This only can be applied to non-extrapolated data.
2. Log-Odds Ratio and Mechanical Factor Threshold: To identify nuclei conforming to RG-associated morphology, we examined the *log-odds ratio* values. This threshold, denoted as F(0), represents the mechanical factor required for RG morphology. Surface plots were generated to visualize this threshold across area (x-axis) and eccentricity (y-axis), and calculated the proportions of data above each threshold. This qualitative approach is particularly useful for analyzing

nuclei that do not meet all model criteria—such as samples with high cell density, including hRG and hNeuron cultures, brain slices, hiPSCs, and heNPCs. Although not all samples exhibit extrapolated data, applying the log-odds ratio exclusively allows us to maximize data use from the experimental set while avoiding potential bias from extrapolated values.

Code Availability and Model Scripts

The primary scripts for constructing, applying, and visualizing the RGM model are available at https://github.com/PepPau/RGM-model-main-scripts.git.

Publicly available single-cell transcriptomics data analysis

To analyze mRNA expression at different developmental stages, we used mouse cerebral cortex single-cell transcriptomics data from a previous study by Di Bella et al.[30] deposited on the GEO database with accession number GSE153162. We used SCANPY[73] to apply quality control filters based on the distribution of counts and genes found on each dataset. We discarded all cells with less than 500 UMIs or more than 50000, all those with less than 800 detected genes and those with more than 7000, and all the cells with more than 15% of mitochondrial content. In total we retained 81792 out of the initial 82415 cells. Subsequently, we discarded an additional 2431 cells that had been identified as doublets by the scrublet package[74]. To retain only cells from relevant developmental stages for our study, we discarded all the cells from E10, E11 and E12. After this selection, we were left with 67961 cells. We then normalized the data using the normalize_total function from SCANPY with a target of 10000 counts per cell, and then we log-transformed the data. We applied dimensionality reduction keeping the first 10 principal components, clustered the data using the Louvain algorithm for community detection[75] (r=0.2) and selected clusters expressing RG-astrocyte lineage markers (Sox2, Pax6, Hes5) and no expression of neuronal (Neurod2, Tubb3, Neurod6, Meg3). We applied again principal component analysis (PCA) on the 14469 selected cells, clustered them on the space of the first 11 principal components and removed those clusters expressing neuronal or oligodendrocyte (Olig1, Olig2, Pdgfra) lineage makers, except for a cluster which expressed both Olig1 and mature astrocyte markers (Aqp4, Slc1a2) (**Figure S3**). After this selection, we retained 9343 that we confidently labeled as RG-astrocyte lineage cells, on which we examined the expression of our proteins of interest.

Pharmacological treatments

Pharmacological inhibition of Ca^{2+}/Calmodulin-Dependent Protein Kinase II (CaMKII) signaling (KN93, 5μM) and non-selective mechanosensing cation channels (GsMTx-4, 1.22μM) was performed for 3h in 3DIV glial cultures grown in control and In2PMMA substrates without previous serum deprivation. As controls, we also treated samples with their respective vehicles: DMSO for KN93 and PBS for GsMTx4. Samples were fixed and prepared for immunocytochemistry assays as previously described. We used two different experiments and the number of cells analyzed were: DMSO, N=1832; KN93, N=1931; PBS, N=1349; and GsMTx5, N=1727.

Calcium Imaging

Glial cultures at 3-4 DIV were positioned in a microfluidic chamber (Open Diamond Bath Imaging Chamber for Round Coverslips; Warner Instruments) and loaded with the calcium-sensitive dye Oregon Green BAPTA-1 AM (OGB-1 AM, Life Technologies, 10 μM in EM to prevent cell detachment) for 30 minutes at 37°C and 5% CO_2. For calcium imaging, the bath solution contained 140 mM NaCl, 5.4 mM KCl, 1 mM $MgCl_2$, 10 mM HEPES, and 10 mM glucose, adjusted to pH 7.4. The bath solution was used under both calcium-free and calcium (2 mM $CaCl_2$) conditions. Intracellular Ca^{2+} activity was recorded over 10 minutes, divided into two phases: an initial 2-minute calcium-free stage to establish baseline activity, followed by 2 mM $CaCl_2$ supplementation.

Imaging was performed on an Olympus IX71 inverted microscope using an XLUMPLFLN 20XW water immersion objective (20x/1, Olympus). OGB-1 AM was excited at 488 nm (50 ms exposure) using a Polychrome V light source (Till Photonics) with a Xenon Short-Arc lamp (Ushio), alongside a 505 nm dichroic beam splitter (Chroma Technology). Emission at 510 nm was filtered with a D535/40 nm emission filter (Chroma Technology) and captured by a C9100-13 EM-CCD camera (Hamamatsu). The emission spectrum shifts in amplitude and peak wavelength upon Ca^{2+} binding, with fluorescence intensity changes indicating free calcium levels, which are quantitatively estimated using the EM-CCD camera. Images were acquired at 1-second intervals at room temperature.

After recording, the recorded area was marked on their back and samples were subsequently washed and incubated in EM at 37°C for 30-60 minutes before fixation and preparation for immunocytochemistry (as described above). For each substrate, eight samples were immunolabeled with Pax6 and nestin markers, although three samples experienced cell loss due to handling, and alignment issues with the recorded area prevented analysis in one sample. Imaging was conducted on a Zeiss LSM 880 spectral confocal microscope with an LD LCI Plan-Apochromat 25x/0.8 Imm Korr DIC M27 objective. Alignment challenges between the 20x objective used in calcium recordings

and confocal objectives necessitated a 0.7x zoom adjustment to match focal planes. Both calcium and confocal images required orientation corrections, and confocal images from In2PMMA samples required flipping due to cell orientation (face-up) (**Figure S8A**).

Calcium Imaging analysis

Calcium signal data was analyzed with a custom-designed MATLAB algorithm to extract nuclear calcium signals in a defined region of interest (ROI). We used ROIs of equal size located on the cell nucleus to mask the image, normalize the signal and quantify the signal magnitude over time. ImageJ snapshots of calcium imaging were co-localized with immunolabeled images to correlate nuclear morphology, expression markers, and calcium signals. A representative cross-correlation is shown in **Figure S8B**.

To quantify relative intracellular calcium levels (fluorescence intensity), background fluorescence was subtracted from each cell's calcium signal at each time point. Background values were obtained by averaging 10 ROIs from cell-free areas at each time point. The background was carefully examined to avoid artifacts (**Figure S9**).

Calcium activity patterns were smoothed using a Savitzky-Golay filter (polynomial order = 2, window size = 6) in Origin Pro v9 (OriginLab, Northampton, MA, USA). **Figure S10** illustrates the raw versus filtered signal. To minimize artifacts, the first 50 frames were excluded, and the signal-to-baseline ratio (SBR) or $\Delta F/F_0$ was calculated using the following formulas:

- $F_0 = \frac{\sum_{i=1}^{50} F_{Baseline}(t)_i}{50}$
- $\frac{\Delta F}{F_0} = \frac{F_i(t) - F_0}{F_0}$

To perform analysis and plots we applied an increase of 100% to the resultant signal, i.e. % = $\frac{\Delta F}{F_0}$ x100.

Statistical analysis

Statistical analysis was performed using IBM SPSS (Version 26), GraphPad Prism version 8.0, R Core Team (2021), RStudio and R: A language and environment for statistical computing (R Foundation for Statistical Computing, Vienna, Austria). We performed the normality test by default and different post-hoc tests depending on the nature of the data. For two sample comparisons we used t-test or Mann-Whitney. For three or more sample comparisons we used one-way or two-way analysis of variance (ANOVA, with Tukey adjustment) or Kruskal-Wallis with multiple comparison test (with

Benjamini-Yekutieli and Krieger FDR correction). To determine differences between populations we performed chi-square tests for 4 groups or multiple regression approach in contingency tables for more than 4 groups adapted from[76]. To demonstrate statistical significance, we deemed it sufficient to utilize thresholds such as p-value < 0.05 and p-value < 0.01. While we frequently observed values lower than 0.001 in numerous instances, we found that adopting a threshold of p-value < 0.01 was satisfactory for identifying meaningful biological distinctions.

BIBLIOGRAPHY

1. Chighizola, M., Dini, T., Lenardi, C., Milani, P., Podestà, A., and Schulte, C. (2019). Mechanotransduction in neuronal cell development and functioning. Biophys Rev *11*, 701-720. 10.1007/s12551-019-00587-2.
2. Fujita, I., Shitamukai, A., Kusumoto, F., Mase, S., Suetsugu, T., Omori, A., Kato, K., Abe, T., Shioi, G., Konno, D., and Matsuzaki, F. (2020). Endfoot regeneration restricts radial glial state and prevents translocation into the outer subventricular zone in early mammalian brain development. Nat Cell Biol *22*, 26-37. 10.1038/s41556-019-0436-9.
3. Ferent, J., Zaidi, D., and Francis, F. (2020). Extracellular Control of Radial Glia Proliferation and Scaffolding During Cortical Development and Pathology. Front Cell Dev Biol *8*, 578341. 10.3389/fcell.2020.578341.
4. Merkle, F.T., and Alvarez-Buylla, A. (2006). Neural stem cells in mammalian development. Curr Opin Cell Biol *18*, 704-709. 10.1016/j.ceb.2006.09.008.
5. Malatesta, P., and Götz, M. (2013). Radial glia - from boring cables to stem cell stars. Development *140*, 483-486. 10.1242/dev.085852.
6. Mihalas, A.B., and Hevner, R.F. (2017). Control of Neuronal Development by T-Box Genes in the Brain. Curr Top Dev Biol *122*, 279-312. 10.1016/bs.ctdb.2016.08.001.
7. Nishiyama, A., Boshans, L., Goncalves, C.M., Wegrzyn, J., and Patel, K.D. (2016). Lineage, fate, and fate potential of NG2-glia. Brain Res *1638*, 116-128. 10.1016/j.brainres.2015.08.013.
8. Zhang, Y., Liu, G., Guo, T., Liang, X.G., Du, H., Yang, L., Bhaduri, A., Li, X., Xu, Z., Zhang, Z., et al. (2020). Cortical Neural Stem Cell Lineage Progression Is Regulated by Extrinsic Signaling Molecule Sonic Hedgehog. Cell Rep *30*, 4490-4504.e4494. 10.1016/j.celrep.2020.03.027.
9. Hunter, K.E., and Hatten, M.E. (1995). Radial glial cell transformation to astrocytes is bidirectional: regulation by a diffusible factor in embryonic forebrain. Proc Natl Acad Sci U S A *92*, 2061-2065. 10.1073/pnas.92.6.2061.
10. Zamboni, M., Llorens-Bobadilla, E., Magnusson, J.P., and Frisén, J. (2020). A Widespread Neurogenic Potential of Neocortical Astrocytes Is Induced by Injury. Cell Stem Cell *27*, 605-617.e605. 10.1016/j.stem.2020.07.006.
11. Yang, J.L., Fan, H., Fu, F.F., Guo, B.L., Huang, Y., Sun, L., Wang, W.T., Xing, J.L., Hu, X.T., Ding, Y.Q., et al. (2023). Transient neurogenesis in ischemic cortex from Sox2. Neural Regen Res *18*, 1521-1526. 10.4103/1673-5374.357910.
12. Ozgun, A., Lomboni, D., Arnott, H., Staines, W.A., Woulfe, J., and Variola, F. (2022). Biomaterials-based strategies for. Biomater Sci *10*, 1134-1165. 10.1039/d1bm01361k.
13. Castillo Ransanz, L., Van Altena, P.F.J., Heine, V.M., and Accardo, A. (2022). Engineered cell culture microenvironments for mechanobiology studies of brain neural cells. Front Bioeng Biotechnol *10*, 1096054. 10.3389/fbioe.2022.1096054.
14. Mattotti, M., Alvarez, Z., Ortega, J.A., Planell, J.A., Engel, E., and Alcantara, S. (2012). Inducing functional radial glia-like progenitors from cortical astrocyte cultures using micropatterned PMMA. Biomaterials *33*, 1759-1770. 10.1016/j.biomaterials.2011.10.086.
15. Alvarez, Z., Sena, E., Mattotti, M., Engel, E., and Alcantara, S. (2014). An efficient and reproducible method to culture Bergmann and cortical radial glia using textured PMMA. Journal of Neuroscience Methods *232*, 93-101. 10.1016/j.jneumeth.2014.05.011.
16. Mattotti, M., Alvarez, Z., Delgado, L., Mateos-Timoneda, M.A., Aparicio, C., Planell, J.A., Alcantara, S., and Engel, E. (2017). Differential neuronal and glial behavior on flat and micro patterned chitosan films. Colloids and Surfaces B-Biointerfaces *158*, 569-577. 10.1016/j.colsurfb.2017.07.045.

17. Kumar, S. (2014). Cellular mechanotransduction: stiffness does matter. Nat Mater *13*, 918-920. 10.1038/nmat4094.
18. Kirby, T.J., and Lammerding, J. (2018). Emerging views of the nucleus as a cellular mechanosensor. Nat Cell Biol *20*, 373-381. 10.1038/s41556-018-0038-y.
19. Kalukula, Y., Stephens, A.D., Lammerding, J., and Gabriele, S. (2022). Mechanics and functional consequences of nuclear deformations. Nat Rev Mol Cell Biol *23*, 583-602. 10.1038/s41580-022-00480-z.
20. Martino, F., Perestrelo, A.R., Vinarský, V., Pagliari, S., and Forte, G. (2018). Cellular Mechanotransduction: From Tension to Function. Front Physiol *9*, 824. 10.3389/fphys.2018.00824.
21. Shao, W., Yang, J., He, M., Yu, X.Y., Lee, C.H., Yang, Z., Joyner, A.L., Anderson, K.V., Zhang, J., Tsou, M.B., et al. (2020). Centrosome anchoring regulates progenitor properties and cortical formation. Nature *580*, 106-112. 10.1038/s41586-020-2139-6.
22. Yanakieva, I., Erzberger, A., Matejčić, M., Modes, C.D., and Norden, C. (2019). Cell and tissue morphology determine actin-dependent nuclear migration mechanisms in neuroepithelia. J Cell Biol *218*, 3272-3289. 10.1083/jcb.201901077.
23. Park, M.G., Jang, H., Lee, S.H., and Lee, C.J. (2017). Flow Shear Stress Enhances the Proliferative Potential of Cultured Radial Glial Cells Possibly Via an Activation of Mechanosensitive Calcium Channel. Exp Neurobiol *26*, 71-81. 10.5607/en.2017.26.2.71.
24. Chi, S., Cui, Y., Wang, H., Jiang, J., Zhang, T., Sun, S., Zhou, Z., Zhong, Y., and Xiao, B. (2022). Astrocytic Piezo1-mediated mechanotransduction determines adult neurogenesis and cognitive functions. Neuron *110*, 2984-2999.e2988. 10.1016/j.neuron.2022.07.010.
25. Niethammer, P. (2021). Components and Mechanisms of Nuclear Mechanotransduction. Annu Rev Cell Dev Biol *37*, 233-256. 10.1146/annurev-cellbio-120319-030049.
26. Ndiaye, A.B., Koenderink, G.H., and Shemesh, M. (2022). Intermediate Filaments in Cellular Mechanoresponsiveness: Mediating Cytoskeletal Crosstalk From Membrane to Nucleus and Back. Front Cell Dev Biol *10*, 882037. 10.3389/fcell.2022.882037.
27. Gurdon, J.B. (1988). A community effect in animal development. Nature *336*, 772-774. 10.1038/336772a0.
28. Mestres, I., Houtman, J., Calegari, F., and Toda, T. (2022). A Nuclear Belt Fastens on Neural Cell Fate. Cells *11*. 10.3390/cells11111761.
29. Wang, M., Ivanovska, I., Vashisth, M., and Discher, D.E. (2022). Nuclear mechanoprotection: From tissue atlases as blueprints to distinctive regulation of nuclear lamins. APL Bioeng *6*, 021504. 10.1063/5.0080392.
30. Di Bella, D.J., Habibi, E., Stickels, R.R., Scalia, G., Brown, J., Yadollahpour, P., Yang, S.M., Abbate, C., Biancalani, T., Macosko, E.Z., et al. (2021). Molecular logic of cellular diversification in the mouse cerebral cortex. Nature *595*, 554-559. 10.1038/s41586-021-03670-5.
31. Elosegui-Artola, A., Andreu, I., Beedle, A.E.M., Lezamiz, A., Uroz, M., Kosmalska, A.J., Oria, R., Kechagia, J.Z., Rico-Lastres, P., Le Roux, A.L., et al. (2017). Force Triggers YAP Nuclear Entry by Regulating Transport across Nuclear Pores. Cell *171*, 1397-1410.e1314. 10.1016/j.cell.2017.10.008.
32. Wagh, K., Garcia, D.A., and Upadhyaya, A. (2021). Phase separation in transcription factor dynamics and chromatin organization. Curr Opin Struct Biol *71*, 148-155. 10.1016/j.sbi.2021.06.009.
33. Sen, B., Xie, Z., Howard, S., Styner, M., van Wijnen, A.J., Uzer, G., and Rubin, J. (2022). Mechanically Induced Nuclear Shuttling of β-Catenin Requires Co-transfer of Actin. Stem Cells *40*, 423-434. 10.1093/stmcls/sxac006.

34. Wrobel, C.N., Mutch, C.A., Swaminathan, S., Taketo, M.M., and Chenn, A. (2007). Persistent expression of stabilized beta-catenin delays maturation of radial glial cells into intermediate progenitors. Dev Biol *309*, 285-297. 10.1016/j.ydbio.2007.07.013.
35. Gao, J., Liao, Y., Qiu, M., and Shen, W. (2021). Wnt/β-Catenin Signaling in Neural Stem Cell Homeostasis and Neurological Diseases. Neuroscientist *27*, 58-72. 10.1177/1073858420914509.
36. Rosenbloom, A.B., Tarczyński, M., Lam, N., Kane, R.S., Bugaj, L.J., and Schaffer, D.V. (2020). β-Catenin signaling dynamics regulate cell fate in differentiating neural stem cells. Proc Natl Acad Sci U S A *117*, 28828-28837. 10.1073/pnas.2008509117.
37. Lavado, A., Gangwar, R., Paré, J., Wan, S., Fan, Y., and Cao, X. (2021). YAP/TAZ maintain the proliferative capacity and structural organization of radial glial cells during brain development. Dev Biol *480*, 39-49. 10.1016/j.ydbio.2021.08.010.
38. Gan, Q., Lee, A., Suzuki, R., Yamagami, T., Stokes, A., Nguyen, B.C., Pleasure, D., Wang, J., Chen, H.W., and Zhou, C.J. (2014). Pax6 mediates ß-catenin signaling for self-renewal and neurogenesis by neocortical radial glial stem cells. Stem Cells *32*, 45-58. 10.1002/stem.1561.
39. Tong, J., Qi, Y., Wang, X., Yu, L., Su, C., Xie, W., and Zhang, J. (2017). Cell micropatterning reveals the modulatory effect of cell shape on proliferation through intracellular calcium transients. Biochim Biophys Acta Mol Cell Res *1864*, 2389-2401. 10.1016/j.bbamcr.2017.09.015.
40. Narendra Talabattula, V.A., Morgan, P., Frech, M.J., Uhrmacher, A.M., Herchenröder, O., Pützer, B.M., Rolfs, A., and Luo, J. (2017). Non-canonical pathway induced by Wnt3a regulates β-catenin via Pyk2 in differentiating human neural progenitor cells. Biochem Biophys Res Commun *491*, 40-46. 10.1016/j.bbrc.2017.07.030.
41. Pathak, M.M., Nourse, J.L., Tran, T., Hwe, J., Arulmoli, J., Le, D.T., Bernardis, E., Flanagan, L.A., and Tombola, F. (2014). Stretch-activated ion channel Piezo1 directs lineage choice in human neural stem cells. Proc Natl Acad Sci U S A *111*, 16148-16153. 10.1073/pnas.1409802111.
42. Gnanasambandam, R., Ghatak, C., Yasmann, A., Nishizawa, K., Sachs, F., Ladokhin, A.S., Sukharev, S.I., and Suchyna, T.M. (2017). GsMTx4: Mechanism of Inhibiting Mechanosensitive Ion Channels. Biophys J *112*, 31-45. 10.1016/j.bpj.2016.11.013.
43. Wong, M.H., Samal, A.B., Lee, M., Vlach, J., Novikov, N., Niedziela-Majka, A., Feng, J.Y., Koltun, D.O., Brendza, K.M., Kwon, H.J., et al. (2019). The KN-93 Molecule Inhibits Calcium/Calmodulin-Dependent Protein Kinase II (CaMKII) Activity by Binding to Ca. J Mol Biol *431*, 1440-1459. 10.1016/j.jmb.2019.02.001.
44. Arjun McKinney, A., Petrova, R., and Panagiotakos, G. (2022). Calcium and activity-dependent signaling in the developing cerebral cortex. Development *149*. 10.1242/dev.198853.
45. Abuwarda, H., and Pathak, M.M. (2020). Mechanobiology of neural development. Curr Opin Cell Biol *66*, 104-111. 10.1016/j.ceb.2020.05.012.
46. Lim, D., Semyanov, A., Genazzani, A., and Verkhratsky, A. (2021). Calcium signaling in neuroglia. Int Rev Cell Mol Biol *362*, 1-53. 10.1016/bs.ircmb.2021.01.003.
47. Weissman, T.A., Riquelme, P.A., Ivic, L., Flint, A.C., and Kriegstein, A.R. (2004). Calcium waves propagate through radial glial cells and modulate proliferation in the developing neocortex. Neuron *43*, 647-661. 10.1016/j.neuron.2004.08.015.
48. Rash, B.G., Ackman, J.B., and Rakic, P. (2016). Bidirectional radial Ca(2+) activity regulates neurogenesis and migration during early cortical column formation. Sci Adv *2*, e1501733. 10.1126/sciadv.1501733.
49. Leclerc, C., Néant, I., and Moreau, M. (2012). The calcium: an early signal that initiates the formation of the nervous system during embryogenesis. Front Mol Neurosci *5*, 3. 10.3389/fnmol.2012.00064.

50. Ortega, J.A., Sirois, C.L., Memi, F., Glidden, N., and Zecevic, N. (2017). Oxygen Levels Regulate the Development of Human Cortical Radial Glia Cells. Cereb Cortex *27*, 3736-3751. 10.1093/cercor/bhw194.
51. Ortega, J.A., Radonjić, N.V., and Zecevic, N. (2013). Sonic hedgehog promotes generation and maintenance of human forebrain Olig2 progenitors. Front Cell Neurosci *7*, 254. 10.3389/fncel.2013.00254.
52. Imamura, O., Pagès, G., Pouysségur, J., Endo, S., and Takishima, K. (2010). ERK1 and ERK2 are required for radial glial maintenance and cortical lamination. Genes Cells *15*, 1072-1088. 10.1111/j.1365-2443.2010.01444.x.
53. Sanchez-Camacho, C., Alberto Ortega, J., Ocana, I., Alcantara, S., and Bovolenta, P. (2011). Appropriate Bmp7 Levels are Required for the Differentiation of Midline Guidepost Cells Involved in Corpus Callosum Formation. Developmental Neurobiology *71*, 337-350. 10.1002/dneu.20865.
54. Ochi, S., Manabe, S., Kikkawa, T., and Osumi, N. (2022). Thirty Years' History since the Discovery of Pax6: From Central Nervous System Development to Neurodevelopmental Disorders. Int J Mol Sci *23*. 10.3390/ijms23116115.
55. Yuste, R., Hawrylycz, M., Aalling, N., Aguilar-Valles, A., Arendt, D., Armañanzas, R., Ascoli, G.A., Bielza, C., Bokharaie, V., Bergmann, T.B., et al. (2020). A community-based transcriptomics classification and nomenclature of neocortical cell types. Nat Neurosci *23*, 1456-1468. 10.1038/s41593-020-0685-8.
56. Miranda-Negrón, Y., and García-Arrarás, J.E. (2022). Radial glia and radial glia-like cells: Their role in neurogenesis and regeneration. Front Neurosci *16*, 1006037. 10.3389/fnins.2022.1006037.
57. Eze, U.C., Bhaduri, A., Haeussler, M., Nowakowski, T.J., and Kriegstein, A.R. (2021). Single-cell atlas of early human brain development highlights heterogeneity of human neuroepithelial cells and early radial glia. Nat Neurosci *24*, 584-594. 10.1038/s41593-020-00794-1.
58. Duran, I., Pombo, J., Sun, B., Gallage, S., Kudo, H., McHugh, D., Bousset, L., Barragan Avila, J.E., Forlano, R., Manousou, P., et al. (2024). Detection of senescence using machine learning algorithms based on nuclear features. Nat Commun *15*, 1041. 10.1038/s41467-024-45421-w.
59. Mattiazzi Usaj, M., Yeung, C.H.L., Friesen, H., Boone, C., and Andrews, B.J. (2021). Single-cell image analysis to explore cell-to-cell heterogeneity in isogenic populations. Cell Syst *12*, 608-621. 10.1016/j.cels.2021.05.010.
60. Smith, K., Piccinini, F., Balassa, T., Koos, K., Danka, T., Azizpour, H., and Horvath, P. (2018). Phenotypic Image Analysis Software Tools for Exploring and Understanding Big Image Data from Cell-Based Assays. Cell Syst *6*, 636-653. 10.1016/j.cels.2018.06.001.
61. Christiansen, E.M., Yang, S.J., Ando, D.M., Javaherian, A., Skibinski, G., Lipnick, S., Mount, E., O'Neil, A., Shah, K., Lee, A.K., et al. (2018). In Silico Labeling: Predicting Fluorescent Labels in Unlabeled Images. Cell *173*, 792-803.e719. 10.1016/j.cell.2018.03.040.
62. Zhu, Y., Huang, R., Wu, Z., Song, S., Cheng, L., and Zhu, R. (2021). Deep learning-based predictive identification of neural stem cell differentiation. Nat Commun *12*, 2614. 10.1038/s41467-021-22758-0.
63. Götz, M., Sirko, S., Beckers, J., and Irmler, M. (2015). Reactive astrocytes as neural stem or progenitor cells: In vivo lineage, In vitro potential, and Genome-wide expression analysis. Glia *63*, 1452-1468. 10.1002/glia.22850.
64. Alvarez, Z., Castano, O., Mateos-Timoneda, M., Planell, J.A., Alcantara, S., and Engel, E. (2014). In vivo reprogramming and vascularization by lactate-releasing biomimetic scaffolds. Journal of Tissue Engineering and Regenerative Medicine *8*, 273.

65. Stipursky, J., Francis, D., and Gomes, F.C. (2012). Activation of MAPK/PI3K/SMAD pathways by TGF-β(1) controls differentiation of radial glia into astrocytes in vitro. Dev Neurosci *34*, 68-81. 10.1159/000338108.
66. Alberto Ortega, J., and Alcantara, S. (2010). BDNF/MAPK/ERK-Induced BMP7 Expression in the Developing Cerebral Cortex Induces Premature Radial Glia Differentiation and Impairs Neuronal Migration. Cerebral Cortex *20*, 2132-2144. 10.1093/cercor/bhp275.
67. Rammensee, S., Kang, M.S., Georgiou, K., Kumar, S., and Schaffer, D.V. (2017). Dynamics of Mechanosensitive Neural Stem Cell Differentiation. Stem Cells *35*, 497-506. 10.1002/stem.2489.
68. Götz, M., Stoykova, A., and Gruss, P. (1998). Pax6 controls radial glia differentiation in the cerebral cortex. Neuron *21*, 1031-1044. 10.1016/s0896-6273(00)80621-2.
69. Schildge, S., Bohrer, C., Beck, K., and Schachtrup, C. (2013). Isolation and culture of mouse cortical astrocytes. J Vis Exp. 10.3791/50079.
70. Mills, C.A., Martinez, E., Errachid, A., Engel, E., Funes, M., Moormann, C., Wahlbrink, T., Gomila, G., Planell, J., and Samitier, J. (2007). Nanoembossed polymer substrates for biomedical surface interaction studies. J Nanosci Nanotechnol *7*, 4588-4594.
71. Bai, J., Liu, K., Jiang, Y., Ying, K., Zhang, P., and Shao, J. (2008). A two-dimensional CVIB imaging system with a speckle tracking algorithm. Ultrasonics *48*, 394-402. 10.1016/j.ultras.2008.01.010.
72. van Tienen, F.H.J., Lindsey, P.J., Kamps, M.A.F., Krapels, I.P., Ramaekers, F.C.S., Brunner, H.G., van den Wijngaard, A., and Broers, J.L.V. (2019). Assessment of fibroblast nuclear morphology aids interpretation of LMNA variants. Eur J Hum Genet *27*, 389-399. 10.1038/s41431-018-0294-0.
73. Wolf, F.A., Angerer, P., and Theis, F.J. (2018). SCANPY: large-scale single-cell gene expression data analysis. Genome Biol *19*, 15. 10.1186/s13059-017-1382-0.
74. Wolock, S.L., Lopez, R., and Klein, A.M. (2019). Scrublet: Computational Identification of Cell Doublets in Single-Cell Transcriptomic Data. Cell Syst *8*, 281-291.e289. 10.1016/j.cels.2018.11.005.
75. Traag, V.A., Waltman, L., and van Eck, N.J. (2019). From Louvain to Leiden: guaranteeing well-connected communities. Sci Rep *9*, 5233. 10.1038/s41598-019-41695-z.
76. Beasley, T.M., and Schumacker, R.a.E. (1995). Multiple Regression Approach to Analyzing Contingency Tables: Post Hoc and Planned comparison procedures. *The Journal of Experimental Education 64* (*nº 1*), 79-93. http://www.jstor.org/stable/20152474.